

1 **Morpho-tectonics of transpressional systems: insights from analog**
2 **modeling**

3 **Ethan M. Conrad^{1,2}, Riccardo Reitano³, Claudio Faccenna^{3,4}, and Thorsten W. Becker^{1,2,5}**

4 ¹Institute for Geophysics, Jackson School of Geosciences, The University of Texas at Austin,
5 Austin, TX, USA.

6 ²Department of Geological Sciences, Jackson School of Geosciences, The University of Texas at
7 Austin, Austin, TX, USA.

8 ³Dipartimento Scienze Geologiche, Università Roma TRE, 00146 Rome, IT..

9 ⁴GFZ German Research Centre for Geosciences Wissenschaftspark "Albert Einstein",
10 Telegrafenberg, 14473 Potsdam, DE.

11 ⁵Oden Institute for Computational Engineering & Sciences, The University of Texas at Austin,
12 Austin, TX, USA

13 Corresponding author: Ethan M. Conrad (econrad@utexas.edu)

14 **Key Points:**

- 15 • Feedback between fault and drainage network development regulates the deformation,
16 exhumation, and morphology of transpressional systems
17 • Increased erosion accelerates the progression from distributed deformation to complete
18 strike-slip strain partitioning
19 • Due to heightened rock uplift and incision, the maximum exhumation in a transpressional
20 wedge is along the master fault and axial valley

21 **Abstract**

22 Transpressional margins are widespread, and their dynamics are relevant for plate boundary
23 evolution globally. Though transpressional orogen evolution involves a topographic response to
24 deformation, many studies focus only on the structural development of the system ignoring surface
25 processes. Here, we present a new set of analog models constructed to investigate how tectonic
26 and surface processes interact at transpressive plate boundaries and shape topography.
27 Experiments are conducted by deforming a previously benchmarked crustal analog material in a
28 meter-scale plexiglass box while controlling erosion through misting nozzles mounted along the
29 transpressional wedge. To analyze the experiments, we generate digital elevation models from
30 laser scans and conduct image correlation analysis on photos taken during experiments. We focus
31 on three experiments that cover a range of erosional conditions and shortening stages (two end-
32 member erosion models and a dry reference). In all experiments, a bivergent wedge forms, and
33 strain partitioning broadly evolves according to previously established models. Regarding
34 drainage networks, we find that the streams in our models develop differently through feedback
35 between fault development and drainage rearrangement processes. Differences between end-
36 member erosional models can be explained by the varying response of streams to structure
37 modulated by rainfall. Additionally, erosion may influence the structural evolution of
38 transpressional topography, leading to accelerated strike-slip partitioning. From these results, we
39 create a model for developing structures, streams, and topography where incision and valley
40 formation along main structures localize exhumation. We apply insights from the models to natural
41 transpressional systems, including the Transverse Ranges, CA, and the Venezuelan Andes.
42

43 1. Introduction

44 Coupling between tectonics and surface processes may affect the localization of deformation
45 and morphological evolution of orogenic systems (e.g., Burbank & Anderson, 2011; Graveleau et
46 al., 2015; Koons, 1995; Molnar & England, 1990; Willett, 1999). When orogenesis is accompanied
47 by a degree of obliquity, the resultant deformation is termed transpression, describing the pairing
48 of wrenching and thrusting structures to accommodate strain (Sanderson & Marchini, 1984). In
49 natural transpressional systems, tectonic strain may be partitioned so that a single vertical strike-
50 slip fault or pairs of strike-slip faults oriented sub-parallel to the zone boundary accommodate the
51 wrench component of oblique convergence (Teyssier et al., 1995). Since most plate boundaries are
52 oblique ($> 10^\circ$ obliquity; Philippon & Corti, 2016), understanding the erosion-tectonic feedback
53 and its relationship with strain partitioning in such settings is essential to accurately constrain,
54 interpret, and model the evolution of the crust and surface.

55 Recent field observations from transpressional settings suggest that climatic variability may
56 affect deformation patterns, exhumation, and topographic change around major faults (Cochran et
57 al., 2017; Cruz et al., 2007). The stream network response to such change may also vary depending
58 on precipitation and bedrock erodibility (Reitman et al., 2022). Generally, faults control drainage
59 geometries through entrainment (Chorley et al., 1984; Koons, 1994, 1995) and preferential incision
60 by mechanical weakening (Koons, 1994, 1995). These mechanisms are important in orogenic
61 systems since fluvial incision is a primary driver of mass transfer. However, a general
62 understanding of how stream networks and fault structure modify the morphotectonic evolution of
63 a transpressional wedge remains to be established.

64 Erosion-tectonic sandbox models provide valuable insight into transpressional systems by
65 combining tectonic deformation and surface mass transport using appropriate analog materials and
66 misting systems that realistically simulate the erosional processes acting on a deforming wedge
67 (Guerit et al., 2016; Guerit et al., 2018). Previous erosion-tectonic models have been used to study
68 the passive rotational response of drainages to oblique convergence (Guerit et al., 2016) and the
69 transient nature of landscapes under transpression (Guerit et al., 2018). Observations from these
70 studies show that streams have a predictable response to deformation in the absence of
71 confounding variables and can be used to characterize deformation in an oblique wedge.
72 Furthermore, analog models by Malavieille et al. (2021) showed that mass transfer by erosional
73 processes could influence the location of major faults, the topographic response to internal
74 deformation partitioning, and, therefore, the long-term evolution of the wedge.

75 Here, we present erosion tectonic sandbox experiments that investigate the relationships
76 between fault structure, stream networks, and the strain field in transpressional systems. We
77 attempt to identify the potential feedback between these components to explain morphological and
78 deformational differences between experimental wedges for high- and low-erosion endmembers.
79 Through analyses of digital elevation models and velocity fields from particle tracking, we address
80 1) how stream networks evolve in transpressional systems under variable erosional conditions, 2)
81 if and how erosion influences the structural and morphological evolution of transpressional
82 mountain belts, and 3) how strain partitioning evolves and is affected by structural and stream
83 network development. The components of wedge evolution related to these questions are
84 highlighted in Figure 1. We extend our results and analyses to natural transpressional prototypes,
85 mainly focusing on the Merida Andes of Venezuela and the central Transverse Ranges along the
86 San Andreas fault system in California, U.S.

87 2. Analog model: Erosion–tectonics sandbox

88 Previous analog studies of the evolution of transpressional mountain belts focus on the
89 structural development of the model without including surface processes (Barcos et al., 2016;
90 Cooke et al., 2020; Lallemand et al., 1994; Leever et al., 2011a,b; Pinet & Cobbold, 1992). Some
91 workers have conducted laboratory studies that included the effects of erosion and sedimentation
92 by removing and applying material by hand (e.g., Bonnet et al., 2007, 2008; Konstantinovskaia &
93 Malavieille, 2005; Malavieille et al., 1993; Perrin et al., 2013). However, this approach limits the
94 internal control of the system. Only a few models combine tectonic stresses and surface processes
95 using misting systems that more realistically simulate the erosional processes acting on a
96 deforming wedge (Graveleau et al., 2015; Graveleau & Dominguez, 2008; Guerit et al., 2016,
97 2018; Lague et al., 2003; Mao et al., 2021; Reitano et al., 2022; Viaplana-Muzas et al., 2015,
98 2019). These “erosion–tectonic” laboratory studies are often limited to purely compressional or
99 extensional settings with few strike-slip (e.g., Graveleau et al., 2015) or transpressional (e.g.,
100 Guerit et al., 2016; Guerit et al., 2018) investigations. In the presented experiments, we add to the
101 current collection of erosion-tectonic studies of transpression and aim to understand how
102 deformation and wedge morphology evolve under the influence of structural and fluvial
103 mechanisms in different erosional regimes.

104 2.1 Experimental material

105 Analog materials used in erosion-tectonic experiments should account for the first-order
106 deformational and erosional behavior of the lithosphere (e.g., Graveleau et al., 2011). In addition,
107 the material should scale appropriately, demonstrating geometric, kinematic, and dynamic
108 similarity (Hubbert, 1951). Many granular single component (e.g., crushed quartz, silica powder)
109 and composite materials (e.g., Mat IV or CM2) have been tested and shown to behave similarly to
110 natural cases in a variety of geodynamic experiments (Graveleau et al., 2011). Our material, CM2,
111 is a combination of 40 wt. % glass microspheres, 40 wt. % silica powder, and 20 wt. % PVC
112 powder hydrated to 20 wt. % H₂O relative to the bulk mixture (Reitano et al., 2020). The water
113 content of the material was measured by mass and volume, knowing the dry density of the material.
114 Reitano et al. (2020) characterized CM2 following the work of Graveleau et al. (2011), who
115 developed a similar material, Mat IV. Mat IV has the same composition as CM2, yet with 18 wt.
116 % PVC and the addition of 2 wt. % graphite powder. These authors show that CM2 and Mat IV
117 deform following the Mohr-Coulomb failure criterion and exhibit basin and channel characteristics
118 akin to nature, including a balance between hillslope diffusion and channel incision. They are also
119 velocity-weakening materials leading to stick-slip. We chose to use 20 wt.% H₂O because at this
120 level, the material is close to saturation; with additional water, the material becomes fluidized and
121 is no longer supported by the grain structure. At saturation, the infiltration capacity (the maximum
122 rainfall rate that the material can absorb) is constant. If the rainfall rate exceeds the infiltration
123 capacity, surface processes must move water through the system (Horton et al., 1933). The
124 infiltration capacity of the material was designed to be minimal by optimizing its porosity,
125 permeability, and grain size distribution (Reitano et al., 2020; Graveleau et al., 2011). The upper
126 layer of the material is rather soft during the experiments but, like the crust, strengthens downward
127 due to compaction and lithostatic pressure. Graveleau et al. (2011) posit that after roughly 1 cm,
128 its mechanical behavior is consistent with frictional values measured at 20 wt. % H₂O. Thus, it is
129 reasonable to assume that once the material package is set, its mechanical behavior is independent
130 of differences in the amount of water delivered to the surface by variable rainfall rates.

131 *2.2 Experimental setup*

132 We conduct experiments in a 2 m × 1 m × 0.5 m plexiglass box, with ends left open for
133 drainage (Figure 2a). The basal slope is fixed at 1° to ensure water exits the system. We set a mylar
134 sheet inside the box and fix a 2 mm thick right-trapezoidal (25 × 100 × 60 × 96 cm) shaped
135 plexiglass board to the sidewall. By pulling the mylar sheet beneath the board, we simulate oblique
136 convergence (Figure 2b). The mylar sheet is pulled by attaching its ends to a wooden plank
137 mounted to a *MecVel screwjack* and Electric Motors *Vela stm* electric motor. We load the board–
138 sheet set up with a ~5 cm thick package of the experimental material hydrated to ~20 wt. % water
139 (see section 2.1). The length and width of the material package are controlled to ensure that the
140 edges do not influence the wedge's evolution or reach the sidewalls of the box. Free boundaries
141 are particularly important on the fixed side of the model as it allows the wedge to form independent
142 of the geometry of a rigid backstop (e.g., Guerit et al., 2016). This independence arises because
143 the material properties, rather than the backstop dip, control the geometry of the wedge.
144 Additionally, the thrust can propagate beyond the location of a would-be backstop.

145 We use the velocity discontinuity between the fixed board and moving sheet to localize
146 deformation, forming a bivergent wedge in the material package. This approach is similar to
147 Leever et al. (2011a,b) and the classic wrench experiments of Riedel (1929), where the velocity
148 discontinuity simulates a basement fault beneath a homogenous sediment cover. We initiate
149 surface processes using misting nozzles mounted on an aluminum crossbar aligned with the wedge
150 trend (Figure 2a). These nozzles maintain a droplet size of fewer than 100 μm to avoid rain splash
151 erosion (Bonnet et al., 2007; Graveleau et al., 2012; Lague et al., 2003; Reitano et al., 2022;
152 Viaplana-Muzas et al., 2015, 2019).

153 *2.3 Parameters varied*

154 We selected three representative experiments (bold font in Table 1) out of six total that
155 explored a more extensive range of rainfall and convergence settings. These additional
156 experiments test the model sensitivity, ensure reproducibility, and explore the parameter space.
157 The experiments were performed with a convergence angle of 20° to investigate wrench-dominated
158 transpression (see Teyssier et al., 1995). Convergence rates ranged from 70 to 320 mm/hr, and
159 rainfall rates from 20 to 34 mm/hr. The three presented experiments provide the most robust and
160 comparable datasets considering the scope of this paper: “dry” (D_62422), “low erosion”
161 (W_71322), and “high erosion” (W_62722). The prefixes D and W are for dry and wet
162 experiments, and the suffix is the date experiments were conducted. In the table, the CR refers to
163 a dimensionless quantity defined as the convergence over rainfall rate (Reitano et al., 2022). An
164 infinite CR means the system is completely dry, whereas a CR of zero indicates the system is not
165 tectonically loaded. Note that here the CR number is only used to organize the models based on
166 the relationship between rainfall and convergence and not for scaling to nature. We present these
167 tests as representative “wet” (“low” and “high erosion”) and “dry” CR scenarios. Throughout the
168 dry experiment, we lightly misted the surface of the material with a spray bottle to keep the material
169 hydrated and its infiltration capacity low. Misting must be done sparingly to maintain the rheology
170 of the medium at its saturation threshold but avoid surface process initiation. Due to the highly
171 differing boundary conditions between the dry experiment with limited misting and the wet
172 experiments with constant misting, the wet experiments are more directly comparable.

173 We consider results robust if the initial fault geometries and the dimensions and general shape
174 of the wedge are reproducible between models. Furthermore, we ensured that throughout the main

175 stages, there was no connectivity between drainages propagating from the edge of the model and
 176 those within the wedge. The latter is necessary because the edge drainages provide a lower base
 177 level. Therefore, once connected with the wedge network, these outlets would localize and increase
 178 the erosion mass flux out of the wedge, dominating the topography and drainage network
 179 morphology (Leopold & Bull, 1979). Within the limitations of erosion-tectonic analog modeling
 180 (e.g., Paola et al., 2009), we show the reproducibility of erosion models by conducting additional
 181 end-member experiments under comparable rainfall and convergence rates (W_62321, W70221,
 182 Figure S1).

183 2.4 Scaling

184 To dynamically scale experiments to natural systems, we should follow the principles
 185 outlined by Hubbert (1937) and Ramberg (1981). However, given uncertainties about the physics
 186 of surface transport, it is not entirely clear how to upscale surface processes. We follow previous
 187 work by only considering geometric and kinematic similarity rather than full dynamic scaling. This
 188 approach might be appropriate if erosional processes are scale-invariant Paola et al., 2009).

189 In terms of geometric comparison with nature, we define a length scaling factor, $l^* =$
 190 l_{model}/l_{nature} . Given the approximate dimensions of transpressional mountain belts ($l = \sim 10^5$ m, $w =$
 191 $\sim 10^4$ m) and that of the wedges generated in the experiment ($l = 1$ m, $w = 10^{-1}$ m), $l^* = 10^{-5}$, meaning
 192 1 cm in the model represents 1 km in nature. To derive the time scaling factor, t^* , we use the
 193 erosion number approach of Reitano et al. (2022), which assumes a steady state between the mass
 194 flux of accreted material and that of eroded material in both model and nature. This assumption
 195 allows one to solve for t^* as $t^* = 4l^*/v^*$, where v^* is the convergence rate scaling factor ($v^* =$
 196 $10^4 \dots 10^5$). From this equation, we estimate $t^* = 4 \times 10^{-10} \dots 4 \times 10^{-9}$, suggesting that 1 hour of
 197 model time corresponds to 30...300 kyr, as in prior work (Graveleau et al., 2011; Mao et al., 2021;
 198 Reitano et al., 2022). In this approach, the t^* equation is the inverted form of that for erodibility,
 199 which has units of time^{-1} . Therefore, the difference in material erodibility, k , between the models
 200 and nature can similarly be evaluated as $k^* = v^*/4l^* = 10^9 \dots 10^{10}$.

201 As discussed in previous works (Graveleau et al., 2011; Paola et al., 2009; Peakall et al.,
 202 1996), it is challenging to downscale geomorphic processes from nature to models. This difficulty
 203 arises because, at present, there is no way to rigorously reduce the dynamic interaction between
 204 fluid media and transported particles due to the range of scales in which surface processes act
 205 (Peakall et al., 1996). Therefore, rainfall rates corresponding to erosion in arid and wet natural
 206 settings cannot be downscaled directly to the experiments. Instead, we present “endmember”
 207 erosion models as those with CR numbers around the upper and lower bounds of what is possible,
 208 given the technical limitations of the material and misting system (Text S1). Considering the
 209 systematic geomorphic variability present in model results (Figure 3; Figure S1) and following the
 210 work of previous authors (Graveleau et al., 2011; Graveleau et al., 2012, 2015; Graveleau &
 211 Dominguez, 2008; Mao et al., 2021; Reitano et al., 2023; Reitano et al., 2022; Reitano et al., 2020;
 212 Strak et al., 2011) we thus consider it appropriate to qualitatively compare the effects of heightened
 213 erosion in the models with those possible in nature.

214 2.5 Analysis

215 We monitor the structural and surficial evolution by scanning the model incrementally with
 216 a laser scanner to create digital elevation models (DEMs) and conducting particle image
 217 velocimetry (PIV) from photos taken every minute. Vertical and horizontal resolutions for the laser

218 are 0.07 mm and 0.05 mm, respectively. Scans are taken at 10 cm, 15 cm, 25 cm, and 35 cm of
 219 convergence. We chose the first increment based on our preliminary experiments, where we
 220 determined that 10 cm of convergence creates sufficient relief (~1 cm) for realistic drainages to
 221 develop. The subsequent increases provide 10 cm increments (+30% shortening) of experiment
 222 evolution up to a maximum of 35 cm (considered 100% shortening). These stages are appropriate
 223 given spatiotemporal constraints, including the influence of edge effects, which grow with rain
 224 time and total displacement. After 35 cm of convergence, especially for high rainfall experiments,
 225 the influence of drainages and faults propagating from the boundary cannot be neglected. We use
 226 the MATLAB software TopoToolbox (Schwanghart & Scherler, 2014) to analyze DEMs and the
 227 corresponding stream networks across the experimental stages. Structural interpretations are made
 228 of each stage by pairing DEMs with photographs, which more clearly display structures lacking
 229 sufficient vertical offset to be resolved by the laser scanner.

230 We derive the evolution of the velocity field using a 2-D cross-correlation technique,
 231 Particle Image Velocimetry (PIV, see Raffel et al., 2007), with the MATLAB toolbox PIVlab
 232 (Thielicke & Sonntag, 2021). However, some unavoidable limitations and high amounts of noise
 233 are associated with using this technique in the presence of a rain system, as surface transport is
 234 also partially tracked, and mist affects the quality of the images. Yet, with a 1-minute capture rate,
 235 image pre-processing, and velocity filtering, PIV can provide insight into the differences between
 236 end member erosional cases. We preprocess images using a contrast-limited, adaptive-histogram
 237 equalization filter and auto-contrast stretch. To generate velocity fields, we use a Fast Fourier
 238 Transform PIV algorithm across a region of interest of 90×30 cm with an initial interrogation
 239 area of 45 mm, three passes down to 12.5 mm, and a Gauss 2×3 point sub-pixel estimator (see
 240 Thielicke & Sonntag, 2021). Resultant velocity fields were calibrated using a photo reference and
 241 analyzed and plotted using Generic Mapping Tools (Wessel et al., 2019). We calculate the
 242 horizontal component of the velocity, u , the maximum horizontal shear strain rates, $\dot{\epsilon}_s$, and the
 243 dilatational strain rate, $\dot{\epsilon}_m$. The strain components $\dot{\epsilon}_s$ and $\dot{\epsilon}_m$ allow us to analyze the localization of
 244 strike-slip and compressional/extensional deformation, respectively. For ease of comparison
 245 between frames of each experiment, we normalize the values by the standard deviation in each
 246 frame and denote the normalized u , $\dot{\epsilon}_s$, and $\dot{\epsilon}_m$ as \hat{u} , $\hat{\epsilon}_s$, and $\hat{\epsilon}_m$, respectively.

247 **3 Results**

248 *3.1 Structural evolution*

249 Figure 3a shows the DEM results of the three presented experiments (dry, low erosion,
 250 high erosion), and Figure 3b shows the interpreted structural evolution of all models. For reference,
 251 we include contrast-enhanced images of the final model stages in Figure 3c-d. To describe our
 252 models, we use the wrench fault terminology of Naylor et al. (1986). Fault progression begins with
 253 the appearance of *en-écheleon* synthetic shears (R , $15^\circ - 30^\circ$) that initiate sub-parallel with the
 254 convergence direction and delineate rhomboidal packages within the wedge. Within the viewing
 255 frames, these features form at least three clear packages, which can be directly compared between
 256 models. R -shears are accompanied by antithetic shears (R' , $65^\circ - 90^\circ$) and connecting splays (S , $>$
 257 17°). The left-lateral displacement of material packages initiates the main inboard (on the fixed
 258 side of the model) thrust (bottommost thrust in Figure 3b), followed by the formation of an
 259 outboard (on the moving side of the model) back-thrust. Together these features form “*pop-up*”
 260 structures, which accommodate the uplift of the blocks. While somewhat obscure in erosional
 261 models due to erosion/sedimentation, a notable low-angle shear striking in the opposite direction

262 (P , $180^\circ - 165^\circ$) forms in all models outlining the bottom-left portion of an elongate diamond-
263 shaped or “pug-nosed” landform (Figure 3a).

264 The main inboard thrust feature moves only a few centimeters during the evolution of each
265 model (2.3 cm, 3.4 cm, and 3.3 cm for dry, low erosion, and high erosion models, respectively).
266 The outboard thrust belt propagates throughout the model at distances depending on the
267 presence/amount of erosion. Thrust sheets nucleate at the tips of the R -shears that extend into the
268 undeformed inboard and outboard sections of the model. With further convergence, lower angle
269 R -shears (Y , $0^\circ - 15^\circ$) form and coalesce with P -shears into an anastomosing velocity discontinuity-
270 parallel master fault zone. In some cases, R' oriented fractures accommodate an extensional
271 component. In either case, these fractures have an apparent clockwise rotation as they are offset
272 by the left lateral R -shear system. R -shears may have an extensional component after they no
273 longer accommodate strike-slip motion, especially when they optimally intersect with the evolving
274 master fault and develop a releasing bend. This occurrence is prevalent in the later stages of the
275 model. R -shears also tend to form arcs concaving into the velocity discontinuity and sometimes
276 form sharp cusps at the velocity discontinuity-fault intersections (Figure 3b). Overall, the structural
277 evolution of the experiments agrees with what is described by prior analog studies of wrench-
278 dominated fault zones (e.g., Casas et al., 2001; Cloos, 1928; Leever et al., 2011a,b; Naylor et al.,
279 1986; Pinet & Cobbold, 1992; Riedel, 1929; Schreurs & Colletta, 1998, 2002; Tchalenko, 1968;
280 Wilcox et al., 1973). Though challenging to interpret, as the material is monochromatic, high-
281 contrast photos of cross sections cut through the high erosion model (Figure 3f, g) show the
282 complex internal deformation within the wedge, interpreted as a thrust-bounded, upward tulip-
283 shaped structure (Figure 3g).

284 To compare the evolution of thrust faults across the models, we show superimposed
285 horizontal topographic slices for each model and stage (Figure 4a). From dry to high erosion, the
286 number of thrust sheets increases at each time stage yet are narrower, forming distinct half-moon-
287 shaped salients. Contrary to the other models, the first thrust sheet that initiates in the high erosion
288 model remains dominant for most of the experiment. This sheet is nearly as wide as the maximum
289 extent of the thrust sheet in the low erosion model and exceeds that of the dry model (3.3 cm).
290 Subsequent thrust initiation in the low erosion model eventually overtakes that of the high erosion
291 model. The maximum thrust toe distance from the velocity discontinuity across all stages is 8.3 cm,
292 11.2 cm, and 10.7 cm for the dry, low, and high erosion experiments, respectively. Thus, the drier
293 systems initiate more yet thinner thrust sheets but still achieve nearly equal or greater cumulative
294 widths at 17 cm, 21 cm, and 16 cm, respectively.

295 There are evident changes in the evolution of the intrawedge strike-slip faults between
296 experiments. We illustrate this in Figures 4b and 4c by extracting the surface traces of these faults,
297 calculating their orientation (Figure 4b), and binning them into rose diagrams (Figure 4c). Dry
298 models show a slight change in the geometry of shears through each stage, with a subtle indication
299 of the eventual through-going, master wrench-fault formation. This final-stage fault seems to
300 reactivate the initial outboard thrust fault plane. Conversely, erosion models show a more
301 significant change in intrawedge shear geometry and an earlier coalescence of shears into a clear,
302 through-going wrench fault. From the inspection of such traces, low-angle faults that begin to
303 merge into the master fault dominate the later stages of the high erosion model. However, faults
304 are more distributed with more R -shears for the low erosion and dry experiments. Visualizing this
305 in the rose diagrams (Figure 4c), the high erosion model has more fault traces ($N = 15$) within 15°
306 of the velocity discontinuity.

307 *3.2 Stream Evolution*

308 Figure 5 shows snapshots of the drainage evolution of the high and low erosion models.
 309 After we engage the rain/mist system, streams nucleate orthogonal to the trace of the thrust sheets
 310 (transverse orientation). As convergence continues, streams evolve following various well-
 311 described mechanisms: headward erosion, drainage deflection by strike-slip motion, drainage
 312 capture, and drainage beheading (see Bishop et al., 1995, for a review). From observations of
 313 pictures and DEMs, it is apparent that faults strongly control the initiation of streams and pathways
 314 of headward erosion. As a result, we generally observe asymmetric forked to rectangular drainage
 315 patterns with consistent spacing and sharp angles defining tributary junctions.

316 Streams that initiate in the *R-shear* direction erode headward throughout the evolution of
 317 the model and follow the reorientation of *R-shears* described above. With the left-lateral deflection
 318 of transverse drainages along *R-shears*, these ‘*R-streams*’ are captured, resulting in sharp cusps in
 319 the drainage topology. This pattern is apparent on both the main thrust and thrust belt sides of the
 320 wedge. However, on the main thrust portion, transverse streams dominate the evolving networks.
 321 In both models, major valleys capture the flow of several transverse streams following the *R-shear*
 322 structures in the low erosion model and the velocity discontinuity-parallel master fault in the high
 323 erosion model. The capture of this valley by transverse tributary drainages causes punctuated
 324 erosion events.

325 In the high erosion model (Figure 5b), the primary drainage system shows less branching
 326 and is more aligned with the velocity discontinuity. Furthermore, *R-streams* initiate early and are
 327 more rapidly captured by transverse streams, resulting in more rectangular drainage networks with
 328 sharper junctions. Similarly, captures are less prevalent in the low erosion model - with one capture
 329 pair (linked blue dots, Figure 5a) compared to eight in the high erosion model at 40% shortening
 330 (Figure 5b). As a result, faults more consistently entrain streams in the direction of structures
 331 forming forked asymmetric drainages. Lastly, as described in section 4.2, the intersection of *R-*
 332 *shears* with the master fault may form a releasing bend, expressed geomorphologically as a
 333 partially restricted lofted valley in our high erosion system.

334 *3.3 PIV analysis of velocities and strain-rates*

335 From the normalized velocities, \hat{u} (Figure 6a), and strain-rates, $\hat{\epsilon}_s$ (Figure 6b), and $\hat{\epsilon}_m$
 336 (Figure 6c), derived through our PIV analysis, we recognize three main phases of strain-rate field
 337 evolution common for all models. In Figure 6d, we extract the structures corresponding to sharp
 338 gradients in \hat{u} (Figure 6a) and related bands of high $\hat{\epsilon}_s$ ($>1.5 \hat{\epsilon}_s$, Figure 6a). Velocities are
 339 particularly useful in verifying shear zones and differentiating them from noise imposed by
 340 landsliding or mist interference (red blobs in Figure 6a).

341 Some early organization phases occur before the first panel in Figure 6, beginning with
 342 distributed deformation followed by shear strain localization along *R* faults at 6...9% shortening
 343 (not shown, stage 1 in Figure 6d). Shortly after, elevated $\hat{\epsilon}_s$ values are focused on the sides of the
 344 wedge (10 cm convergence or 30 % shortening), marking a phase of incomplete partitioning and
 345 oblique faulting on the major thrust structures (stage 2 in Figure 6d). The experiments then enter
 346 a transitional stage (stage 3 in Figure 6d). Synchronous with the structural evolution, strike-slip
 347 motion becomes increasingly localized on a narrow band of anastomosing strike-slip faults
 348 (Figure 6c). The high erosion experiment achieves near-complete strike-slip strain partitioning at
 349 70% shortening (stage 4 in Figure 6d). We consider a system to be partitioned if there is a single

350 continuous band of $> 1.5 \hat{\epsilon}_s$. For the other experiments, a strain rate scenario resembling complete
 351 strike-slip partitioning is not reached until the final frame (35 cm or 100% shortening). This
 352 difference suggests that the strain partitioning evolution is accelerated in the high erosion model.
 353 The more prevalent noise from land sliding attests to more vigorous sediment routing out of the
 354 wedge. Balanced by compression at the boundaries, the interior of the wedge is under extension in
 355 each model and stage (Figure 6c). This band becomes localized to the master-fault zone as the
 356 models progress and compression becomes less organized. Additionally, more red anomalies
 357 (restraining bends?) within blue extensional bands occur along the master-fault zone in the dry
 358 model compared to wet models.

359 3.4 Topographic evolution

360 Initial topography forms along pop-up structures as rhomboidal slices (Figure 3). With the
 361 onset of thrust belt propagation, the topography develops transverse asymmetry, with one steep
 362 side corresponding to the main thrust and a broader side corresponding to the thrust belt. As can
 363 be seen from the differences between the dry and erosion models, hillslope diffusion and stream
 364 erosion drastically modify the topography by incising valleys and causing fault scarps to retreat
 365 inward toward the velocity discontinuity. Alluvial fans fill the recessed portions of ridges. As
 366 expected, there are broader and higher volume alluvial fans and more deeply incised channels in
 367 the high erosion model (Figure 3c-e). In the dry model, the final topography resembles an uplifted
 368 and broadly concave plateau. With increased erosion, the topography is more rugged and
 369 characterized by steeper peaks and more incised valleys. The topographic evolution of each model
 370 is captured in Figure 7a-c showing the changing maximum and mean width, elevation, and thrust
 371 belt gradient (elevation divided by distance from velocity discontinuity) across shortening stages.
 372 In all experiments, the maximum and mean values show similar trends. Thus, we will only discuss
 373 the mean, with the maximum serving as an upper bound. We calculated the mean width and
 374 distance from the velocity discontinuity by averaging the difference between 1,000 corresponding
 375 points on the inboard and outboard thrusts and velocity discontinuity, respectively.

376 Figure 7a shows the changing width of the wedges. The high erosion model shows an
 377 increase in width of ~ 4 cm after the first erosional stage, then a plateau with continued
 378 convergence. On the other hand, the low erosion model width increases by ~ 3 cm and continues
 379 to grow as the experiment continues. The dry model has a broader initial topography and shows
 380 slow and steady growth in the wedge width from 12 to 14 cm (Figure 7a). As the experiment
 381 evolves, it is marked by a higher curvature thrust belt and more salients and recesses. Furthermore,
 382 there is no channel incision, resulting in a broad wedge dissected only by strike-slip structures.
 383 The characteristic diamond or pug-nose shape of wrench-dominated systems is most evident in the
 384 dry model due to the intersection of *P* and *R-shears* (Figure 3a). With increased erosion, structures
 385 that do not accommodate significant displacement become less apparent. For instance, in the
 386 erosion models, the scarp of the uplifted *P* and *R-shears* that delineate the diamond structure is
 387 eroded in the outboard direction, nearly hiding the feature altogether. There are also differences in
 388 relief across strike-slip faults between models. For the high erosion model, *Y* structures have more
 389 relief. In the dry and low erosion model, relief is higher on *R* structures.

390 The surface uplift seems to progress similarly in all models, with only subtle differences in the
 391 rate and magnitude. From zero to 25 centimeters, each experiment shows an initial phase of more
 392 rapid uplift (3...3.5 cm at 25 cm of convergence) followed by a slow rise, perhaps approaching a
 393 limit of around 4 cm (Figure 7b). Figure 7c shows the elevation of the wedge divided by the

394 distance of the thrust toe from the velocity discontinuity. The inverse tangent of the plotted values
 395 is effectively the slope of the thrust belt. Using a thrust belt dip of 25°...35° and the peak angle of
 396 internal friction, ϕ , of wet CM2 ($\phi = 25^\circ \dots 36^\circ$, from Reitano et al. 2020), the error window for the
 397 inverse tangent of the theoretical slope angle, α , from critical taper theory (Dahlen, 1990) is $\alpha =$
 398 $15^\circ \dots 26^\circ$. The tangents of these alpha windows, α' , are plotted in Figure 7c ($\alpha' = 0.27 \dots 0.49$).
 399 Initially, the thrust belt slope in the dry and low erosion models increases into the α window. In
 400 contrast, the wedge slope in the high erosion model is stable at first, corresponding to the early
 401 propagation of a wide thrust sheet. All models reach a value of approximately 0.3 at 70%
 402 shortening. From 70% to 100% shortening, the wedge slope reaches a steady state in the wet
 403 models. In contrast, in the dry model, it continues to steepen.

404 A swath section of the evolution of the high erosion model is shown in Figure 7d, highlighting
 405 the occurrence of the velocity discontinuity-parallel valley and magnitude of stream incision. In
 406 this view, erosion by transverse streams is captured by the width of the colored area, while valleys
 407 along the section represent erosion by longitudinal streams. To provide a picture of the localization
 408 of exhumation across the profile, we isolated the swath profile at 100% shortening and found a
 409 line that captured local maxima and flat portions along the swath maximum (Figure 7e). This line
 410 may represent a rough estimate for rock uplift, assuming rock uplift is minimal. We then estimate
 411 the total exhumation driven by transverse and longitudinal stream incision as the difference
 412 between the rock uplift envelope and upper and lower swath bounds. There are four locations
 413 where a maximum exhumation value of 7 mm is reached. The minimum exhumation at some of
 414 these points ranges from 0...5 mm, depending on the presence of an incising longitudinal stream.

415 **4 Discussion**

416 *4.1 Drainage evolution in response to transpressional tectonics*

417 Considering the experimental results (Figure 5) and the modes of drainage reorganization
 418 described in the literature (e.g., Bishop, 1995; Bloom, 1998; Castelltort et al., 2012; Hallet &
 419 Molnar, 2001; Koons, 1994, 1995; Ramsey et al., 2007), we group stream response mechanisms
 420 to tectonic deformation into two categories:

- 421 1. a dynamic reorganization response influenced by the structural evolution of the orogen.
- 422 2. a passive response to local strain.

423 The primary drainage rearrangement mechanisms that enable the dynamic reorganization
 424 response to structure are entrainment by fault block growth, diversion and beheading by lateral
 425 displacement, and lengthening and capture by headward erosion and preferential fault plane
 426 incision (Bloom, 1991; Koons, 1994, 1995; Bishop, 1995). Figure 8a-j shows several examples of
 427 these dynamic responses. The evolution of each drainage network can be considered the result of
 428 the linear combination of these mechanisms.

429 Differences in stream network geometry between erosion models suggest that the rate at which
 430 the drainage system responds to structure controls the potential feedback with structural evolution
 431 (Figure 5). More erosive conditions (headward erosion, capture) favor some dynamic stream
 432 response mechanisms and, thus, a shorter response time to structural change. However, other
 433 mechanisms, such as deflection and preferential incision, rely on more structurally dominated
 434 stream paths (Koons et al., 1994). In Figure 5, drainages in the high erosion model respond more
 435 quickly to the structural evolution of the model and deflection in the direction of *R*-shears, with a

436 response evident at 70% shortening. There are also more capture pairs at 40% and 70% shortening,
437 with 12 in the high erosion model compared to 6 in the low erosion model. Due to this heightened
438 response, high erosion stream networks are more rectangular, and a clear axial valley forms with
439 4-6 mm of incision. Alternatively, streams in the low erosion model have a more delayed response
440 forming asymmetric forked drainage networks in the final stage. To highlight these differences, in
441 Figure 8k, we show single characteristic drainage basin networks from both the high and low
442 erosion models.

443 The processes described above may explain the formation of a more incised axial valley by
444 drainage redirection in the high erosion model (Figure 5) due to higher strain localization on the
445 master fault (Figure 6b) and pervasive along-strike extension (Figure 6c). The material in these
446 shear zones is weakened by the concentration of mechanical strain and erosional energy along fault
447 damage zones as a function of the strain-weakening behavior of the material (Vermeer & De Borst,
448 1984). Such strain-weakening behavior was described in the material characterization of Reitano
449 et al. (2020). In both cases, vertical offsets along main structures (1 mm – 10 mm) entrain streams
450 so that they reflect the orientation of the active fault system, especially at later stages once
451 extension becomes concentrated on the master fault, and the stream-structure feedbacks are well-
452 developed.

453 Once deeply incised, streams may also rotate with the local strain field, described here as
454 the passive response to local strain (Castelltort et al., 2012; Goren et al., 2015; Guerit et al., 2018;
455 Hallet & Molnar, 2001; Ramsey et al., 2007; Zeitler et al., 2001). In both the high and low erosion
456 models, the passive response is less commonly observed but nevertheless tracks the anticlockwise
457 rotation of some blocks up to a few degrees (Figure 5). The stepwise left-lateral deflection of
458 stream segments (Figure 8e) further assists the apparent rotation.

459 For a stream to be a passive strain marker, the initial orientation of streams should be nearly
460 perpendicular to the trend of the wedge, so they are ideal for rotation with the strain-rate field and
461 can be reliably measured. The initial orientation of such streams seems to be controlled by the R'
462 fracture structure. These streams follow the nucleation and rotation of R' fractures ($< 10^\circ$) with
463 continued convergence (Figure 5a). Passive streams must also be in a place where shear strain is
464 distributed equally across their length because shear strain is localized differently depending on
465 the stage of the experiment. Therefore, even with poor fault exposure, streams can provide insight
466 into where shear strain is localized in a wedge and how mature the orogen is regarding the
467 evolution of strike-slip partitioning.

468 *4.2 Links between fault structure, erosion, and the evolution of strain partitioning*

469 In general, the structural and strain partitioning results of our experiments agree with previous
470 experiments using dry quartz sand (e.g., Leever et al., 2011a; Pinet & Cobbold, 1992; Schreurs &
471 Colletta, 1998) and wet kaolin clay (Cooke et al., 2020). Variations in our results may be attributed
472 to the tested convergence angle, the rheology of the material, erosion, and the approach to fault
473 initiation. Using a similar velocity discontinuity approach, Leever et al. (2011a) built on the work
474 of Pinet & Cobbold (1992), describing a 3-stage evolution of the strain field during transpression
475 from distributed strain to full partitioning. Expanding the work of these authors, we describe the
476 progression observed in our models (Figure 6) by combining wrench tectonics within the wedge
477 (e.g., Naylor et al., 1986; Tchalenko, 1970; Wilcox et al., 1973) with the evolution described by
478 Leever et al. (2011a).

479 Beginning with stage 1, following the period of distributed strain, strike-slip deformation is
 480 first accommodated along *R*-shear structures, as the principal infinitesimal strain axes are
 481 horizontal in wrench-dominated transpression (Tikoff & Teyssier, 1994). This order of fault
 482 formation (*en-échélon* *R*-shearing before thrusting) is also documented in previous experiments
 483 using differing rheologies under low-angle transpression (Cooke et al., 2020; Schreurs & Colletta,
 484 1998). In stage 2, a slow-growing thrust forms on both sides of the velocity discontinuity,
 485 eventually resulting in a bivergent wedge (30% shortening in presented models). The complete
 486 formation of thrust structures bounding the material packages provides pervasive discontinuities
 487 in the system where oblique motion preferentially concentrates. The system then enters stage 3, a
 488 transitional stage (40% shortening in presented models), where low-angle structures ($< 17^\circ$ to the
 489 velocity discontinuity) and splay faults form, grow, and eventually link (see Naylor et al., 1986 for
 490 discussion). Stage 4 begins when a velocity discontinuity-parallel anastomosing “master fault”
 491 zone becomes apparent. Synchronously the zones of extension and principal shear narrow over the
 492 velocity discontinuity (70% and 100% shortening in high and low erosion models, respectively).
 493 Subsequent deformations are mostly independent, and bivergent thrusts now have a purely velocity
 494 discontinuity perpendicular dip-slip component, while the master fault system fully accommodates
 495 the strike-slip component of bulk strain.

496 We observe the above stages of strain evolution across all the presented models (Figure 6).
 497 However, the difference in shortening between when the high and low erosion models enter stage 4
 498 suggests that strain partitioning is also dependent on the erosion/rainfall rate relative to the
 499 convergence rate. By 70% shortening in the high erosion model, a velocity discontinuity-parallel
 500 master fault system is evident (Figure 4b, c) with well-developed strike-slip partitioning (Figure 6).
 501 In the low erosion model, while there is an indication that these paired features are developing, the
 502 structure is geometrically and kinematically immature – in the context of a fully connected
 503 anastomosing master fault zone with localized strike-slip deformation. For the dry model, the
 504 velocity discontinuity-parallel strike-slip system is well-formed by 100% shortening with $\hat{\epsilon}_s > 1.5$,
 505 yet there is also $> 1.5 \hat{\epsilon}_s$ on the outboard thrust.

506 The development of shear zones in the high erosion model coincides with the development of
 507 an axial valley. This observation suggests that the accelerated progression of the model through
 508 the stages of strain partitioning is linked to the erosion of fault scarps and incision by structurally
 509 controlled drainages. Therefore, feedback between the evolving stream and fault networks may
 510 accelerate strain partitioning in more erosive systems. The entrainment of streams by major faults
 511 leads to preferential incision along these structures and a positive interference with *Y*-shear
 512 formation through drainage capture, ultimately leading to the earlier appearance of a fully
 513 partitioned master wrench fault. This series is shown in Figure 4c by the increase in the 0° - 15° bin
 514 and Figure 5b by the incision of a velocity discontinuity parallel drainage along the trace of the
 515 master fault and capture of the headwaters of adjacent streams.

516 We discuss two potential explanations for the earlier formation of a velocity discontinuity-
 517 parallel valley and earlier strike-slip partitioning: 1) focused mass removal by incision changing
 518 the stress balance in the material, thus exposing and localizing deformation earlier along actively
 519 developing *Y*- and *P*-shears, and 2) weakening of the fault by infiltration and water-induced friction
 520 reduction.

521 Considering the overburden removal mechanism, in a wedge loading scenario, there is a
 522 balance between tectonic forcing, fault friction, and the overburden due to topography. While local
 523 stress states may be complex, we can gain some insights by considering the surface transport-

524 associated overburden modification, i.e., the unclamping due to the perturbation in pressure, $\Delta P =$
 525 $\rho g(h_0 - h)$, where ρ is the density of the material, g is the acceleration due to gravity, h_0 is the
 526 thickness of the wedge with no erosion, and h is the thickness of the wedge with erosion. Thus,
 527 given the density of the material is constant, the relative unclamping is simply, $h_0/(h_0 - h)$. To
 528 estimate this for the wet models, given variable across-trend incision patterns, we evaluate 5 cm
 529 wide swath profiles at 70% shortening, with a centerline across the midsection of the innermost
 530 rhomboidal package. We then consider the change in wedge thickness by erosion to be the
 531 difference in maximum and minimum elevations across the length of the swath profile. These
 532 values range from 0.5...8.5 mm and 0.25...6 mm for the high and low erosion cases, respectively.
 533 Thus, compared to the wedge thickness without erosion (maximum elevations across the swath on
 534 a 5 cm thick material package), there is an overall overburden reduction of up to 11%, with a
 535 maximum difference of ~3% between high and low erosion cases. While this change need not
 536 translate directly to fault stress mediation, Cooke et al. (2020) observe similar unclamping in
 537 transpression experiments using kaolinite clay, positing that increased slip on the wedge-bounding
 538 thrust results in extension in the hanging wall and unclamping of the strike-slip fault. Furthermore,
 539 since the initial slip style of the wedge-bounding thrusts is initially oblique, the reduction in vertical
 540 stress by erosion also assists in the rotation of the stress field so that the least principal stress is
 541 vertical, and the fault behaves as purely dip slip. The different stress states in the dry versus wet
 542 cases may also explain the observation that the models with erosion reach a steady state by ~70%
 543 shortening, yet the dry case does not until perhaps after ~100% shortening (Figure 7). While 11%
 544 is a relatively small fraction, the effect of unloading is sustained over the model run, and we
 545 consider a modified mechanical state due to unloading a plausible explanation of the observed
 546 strain localization.

547 The second mechanism, H₂O-related weakening, suggests that local differences in water
 548 content around faults in erosion models may reduce their strength. Faults in the model may provide
 549 pathways for fluids to enter, especially in the later stages, when extension along the master fault
 550 may provide additional space where water can more easily penetrate the material at depth.
 551 However, frictional weakening by fluid infiltration and pressurization only applies to a confined
 552 system (Terzaghi, 1943). Since faults in our model are surrounded by a permeable media, there
 553 should be no significant component of weakening by pore-fluid pressurization, as water can escape
 554 freely. A second H₂O-influenced consideration is that differences in internal friction by variable
 555 bulk water content may affect the angle at which faults initiate. According to the Coulomb-Mohr
 556 criterion, shears form at $45^\circ - \phi/2$ to the first principal stress, first with R shears, then later lower
 557 angle Y and P shears as the stress field rotates (Naylor et al., 1986). Therefore, if ϕ is lower, faults
 558 would initiate at a lower angle. Also, Burbidge and Braun (1998) suggest that ϕ affects the critical
 559 obliquity for partitioning, where a lower ϕ allows strain partitioning to develop at lower
 560 convergence obliquities. Thus, partitioning should develop more quickly when ϕ is low. However,
 561 given the low infiltration capacity of the material and that it is saturated at the outset of the
 562 experiments, there should be no substantial difference in water content for the bulk material
 563 package between erosion models. Thus, based on the fundamental material characteristics, we
 564 assume that the effect of the amount of water delivered by misters on differences in the evolution
 565 of strain partitioning in the models is minor.

566 *4.3 Coupling between fault and stream networks to shape topography*

567 In an oblique collision zone, the topography of the resulting mountain belt is that of a thrust
 568 bounded wedge. Relief is generally subdued but rises abruptly into a steep backslope to the main

569 divide, which falls steeply to the indenter forming the inboard slope (Koons et al., 1994). We
 570 observe the same general morphology in our models (Figure 3). Yet, at shorter length scales (< 5
 571 cm), there are apparent differences between the dry, high, and low erosion models. Here we argue
 572 that these topographic variations between our models depend on this faulting-surface process
 573 feedback and its impact on strain partitioning.

574 The interplay between tectonic and erosional factors manifests in part as the trends we see in
 575 the lateral growth of the wedge between different models (Figures 3, 4, and 7; cf. Dahlen & Suppe,
 576 1988; Steer et al., 2014). The high erosion model has fewer, yet wider, thrust sheets. The width of
 577 these sheets is a function of gradual thickening by syntectonic deposition of alluvium and more
 578 rapid and widespread erosion, leading to the preferential propagation of the basal thrust further
 579 away from the wedge and reduction of surface slope (Bonnet et al., 2007; Fillon et al., 2013;
 580 Malavieille, 2010; Reitano et al., 2022; Simpson, 2006; Stockmal et al., 2007). The formation of
 581 additional thrusts is also delayed due to the crustal thickening. Thus, further shortening is required
 582 to propagate deformation into the foreland. In contrast, the low erosion model continues to expand
 583 with the formation of thrust sheets and outpaces the growth of the high erosion model. The width
 584 of a wedge in an oblique system is further affected by lateral block motion along *R*- and *Y*-shears.
 585 The bookshelf-style faulting along these features generally reduces the width of the wedge, linking
 586 the width of the wedge to the degree of strain partitioning.

587 In Figure 7, for the models including erosion, the relationship between surface uplift and wedge
 588 propagation is well explained by the critical taper model (Dahlen, 1990). In these experiments, the
 589 wedge reaches a critical state by 70% shortening. At this point, material accretion is fully balanced
 590 by erosion out of the wedge and the wedge ceases to grow (Hilley & Strecker, 2004; Willett, 1999).
 591 The onset of a steady state condition coincides with the appearance of a fully strike-slip partitioned
 592 master fault with a component of dilation and the establishment of a subparallel main axial or *R*-
 593 shear drainage. Conversely, in the dry model, wedge widening stabilizes by 60% shortening
 594 (Figure 7a), yet a critical state is never fully attained (Figure 7c). This observation suggests that
 595 the stream-fault feedback is fundamental in achieving an erosional steady state condition.

596 The location and amplitude of salients and recesses in the thrust belt are also controlled by the
 597 along-trend distribution of erosion (Graveleau & Dominguez, 2008; Liu et al., 2020; Marshak,
 598 2004). Erosion and sedimentation are localized where the tips of *R* shears intersect the outermost
 599 thrust. At these locations, the wedge is driven back to a supercritical state, potentially limiting
 600 thrust propagation. Such interactions may also help explain the relatively slow wedge growth in
 601 the high erosion model. Since structurally controlled drainages develop more rapidly, they
 602 concentrate sediment discharge and hamper wedge growth (Liu et al., 2020).

603 The swath profiles from the high erosion model shown in Figure 7d highlight how erosion,
 604 incision, and deformation modify the elevation and relief of the wedge at different shortening
 605 stages. The measurements given in Figure 7e capture the spatial exhumation patterns across the
 606 wedge by separating the contributions of transverse and longitudinal stream incision to exhume
 607 material. Maximum exhumation is reached in four locations across this profile, which, given an l^*
 608 of 1×10^{-5} , translates to 700 m of exhumation in nature and with a t^* of $4 \times 10^{-10} \dots 4 \times 10^{-9}$, an
 609 exhumation rate of 0.5 ... 5 km/Myr. This value is reasonable given the global range of long-term
 610 exhumation rates (e.g., Granger, 2007; Hecht & Oguchi, 2017, and references therein).

611 There are informative differences in the minimum values for the locations where exhumation
 612 reaches a maximum. A minimum of zero (e.g., position 4 in Figure 7d) suggests transverse stream

613 incision is the dominant exhumation mechanism and is thus a local signal. Conversely, a value
614 close to the maximum (e.g., position 2 in Figure 7d) means that exhumation is continuously high
615 along strike. In other words, exhumation in a transpressional setting is greatest where the major
616 trunk streams intersect the velocity discontinuity because both transverse streams and the
617 longitudinal valley contribute to exhuming rock. Furthermore, the later capture of this main valley
618 by transverse streams, as posited for transpressional systems by (Babault et al., 2012), would
619 modify the sediment routing and transiently accelerate erosion (Bishop et al., 1995). As observed
620 in Figure 5, the location of these transverse streams is likely controlled by the *R*-shear structure.
621 Thus, in thermochronometric studies, we might expect the youngest dates at these intersections.

622 Our results indicate that the morphology of a transpressional wedge is linked to the systematics
623 of the potential feedback between faulting and incision. Specifically, valley orientation and shape
624 vary based on the amount of precipitation/erosion, the geometry of drainage networks, and the
625 degree and duration of strike-slip partitioning. Figure 9 synthesizes the evolution of stream and
626 fault networks, strain partitioning, and topography between high and low erosion systems. The
627 synthesized stages described here follow an initial stage of distributed strain and correspond to the
628 strain evolution stages in section 4.2.

629 **Stage 1 (pre-erosion):** *R*-shear structures accommodate strike-slip deformation and link
630 laterally along thrust structures.

631 **Stage 2:** With the onset of erosion, transverse streams form along uplifted rhomboidal
632 packages. Streams are mainly offset along wedge-bounding thrusts since, at this stage, they
633 accommodate both the strike-slip and velocity discontinuity-perpendicular components of
634 deformation.

635 **Stage 3:** A transitional phase when drainages actively respond to the progressive evolution of
636 faults toward parallelism with underlying velocity discontinuity or passively rotate with simple
637 shearing. Ridges and valleys transiently develop following the fault-stream feedback and
638 progression toward complete partitioning. As controlled by the critical taper of the wedge, thrust
639 sheets begin to form and propagate as a function of erosion rate and strike-slip displacement on *R*-
640 shears. The low erosion model has more but thinner thrust sheets. In comparison, in the high
641 erosion scenario, a wide thrust sheet forms early on and accommodates most convergence
642 throughout the model evolution. The high erosion model also has more low-angle strike-slip
643 structures (*Y* and *P* shears). Within a radius equal to the wavelength of the dominant valleys
644 (~5 cm), the local topography along these structures exceeds 5 mm, the highest for incised valleys
645 in the models. These deep valleys indicate that the collocated trunk streams and shears are
646 significant incision points. Sediment routing out of these incised valleys locally induces a
647 supercritical state in the wedge, limiting its propagation in the near field.

648 **Stage 4:** The wedge is fully partitioned with a well-developed master fault system. The main
649 drainage is created by stream entrainment along the master fault forming a distinct axial valley.
650 High volumes of sediment are routed out of orogen along this valley, and exhumation is localized.
651 This phase is reached at lower shortening in the high erosion model due to the accelerated erosion-
652 strain partitioning feedback. The rapid evolution of strain partitioning is facilitated by heightened
653 incision and headward erosion, more vigorous stream reorganization, and mass removal along
654 stream networks. For streams in the low erosion model, deflection, diversion, and erosion along *R*
655 structures lead to asymmetric forked stream networks that curve into the wedge in the direction
656 parallel to the convergence vector. In contrast, streams in the high erosion model are more

657 rectangular, reflecting the more prevalent capture mechanisms and the change in prevailing
658 structures from *R* to the more velocity discontinuity-parallel *Y*-shears and master fault.

659 **Post strain partitioning and wedge development:** Kinematic separation of rhomboidal
660 landforms along the master fault–main valley feature with continuous strike-slip deformation and
661 exhumation along the master fault system.

662 4.4 Comparison with natural systems

663 Our models have numerous simplifications, including the absence of a more ductile lower
664 crust, which we know affects strain localization (e.g., Roy & Royden, 2000a, b). Moreover,
665 because our experiments couple nonlinear deformational and topography forming processes, it is
666 challenging to extrapolate observations made within the time frame of experimental systems or
667 over the seismic cycle to the deformation patterns observed in large and long-lived collisional
668 zones. While attempts have been made, there is still work to be done to fully characterize the
669 scaling of the material transport processes and the material’s deformational behavior (see
670 section 2.1).

671 Concerning the boundary conditions, at depth, the velocity discontinuity set-up and activation
672 of slip along the basement fault idealizes the propagation of a fault from a basement structure to
673 an undeformed homogenous cover. Furthermore, there may be edge effects on the side of the shear
674 zone, affecting the drainage patterns at later stages. These effects result from offsetting one side
675 of the material package and exposing void space against the evolving orogen. Lastly, we ignore
676 the impact of some erosional processes and modifiers, with examples including glaciation and
677 vegetation.

678 Given those assumptions, the patterns in the models presented here still provide some insights
679 into fault development and propagation, strain partitioning, dynamic river network processes, and
680 topographic formation in transpressional orogens. There are several active or recently active
681 transpressive systems around the globe where the results of this study are relevant. Some of many
682 include the Central-Western Colombian Andes (Figure 10a; Cortés et al., 2005; Suter et al., 2008),
683 the Merida Andes in Venezuela (Figure 10b; Audemard & Audemard, 2002; Erikson et al., 2012),
684 and the central Transverse Ranges along the San Andres fault system (Figure 10c; Binnie et al.,
685 2008; Blythe et al., 2002; Matti & Morton, 1993). The climatic setting for each of these examples
686 differs, with annual precipitation rates of 200–300 cm/yr in the Central–Western Colombian
687 Andes, 50–250 cm/yr in the Merida Andes, and 25 – 100 cm/yr in the Central Transverse Ranges
688 (estimated from WorldClim2, Fick & Hijmans, 2017). The key morphostructural similarities
689 between each natural prototype and presented models are exhibited in Figure 10.

690 Curiously, the early-stage macroscopic topographic features we observe only exist in some of
691 these orogens. Notably, orogen-scale repeated *R*-shear structures occur in few locations of wrench-
692 dominated deformation (e.g., Tchalenko & Ambraseys, 1970). Based on experiments and natural
693 observations, Keller et al. (1997) posit that *P*-shears dominate over *R*-shears in zones of oblique
694 convergent deformation. The rarity of *R*-shear structures is likely linked to the varying kinematic
695 modes of bulk strain accommodation in zones of transpressional deformation due to lithological
696 complexity, pre-existing structural anisotropy, convergence angle, poor relief on faults or nearfield
697 sedimentation, and climatic control.

698 Furthermore, as shown in experiments from the literature, *en-échélon R* features are short-lived
699 structures considering the long-term evolution of an orogen (Wilcox et al., 1973), and thus, so is

700 the time scale to complete strain partitioning. As follows, *en-échelon* strike-slip structures should
701 be observed only in tectonically young orogeny (< 10 Myrs) with relatively consistent rheology
702 and constant convergence angles across the zone. In other words, the global examples of
703 transpressional tectonics only provide a snapshot of the overall evolution of a transpressional
704 wedge. Thus, the rapid progression through the initial stages biases observations toward the final
705 *R*-shear-absent configurations.

706 For the evolution and later topographic expression of transpression in nature to strongly
707 resemble our experiments, the region must also have a nearly single-phase tectonic history with a
708 limited amount of inherited structural anisotropy. The convergence angle also plays a significant
709 role. At low obliquities, there is little to no strike-slip partitioning, while at high obliquities, such
710 as along the San Andreas fault system (Figure 10c), there are high degrees of strike-slip
711 partitioning (Teyssier et al. 1995). The first-order differences in the structural style, degree of
712 partitioning, and morphology between each of these examples are likely related to this point, as
713 the estimated convergence angles are different for each of the examples presented in Figure 10 at
714 60° for the central and western Colombian Andes, 25° for the Merida Andes (Mora-Páez et al.,
715 2019) and 30° for the central Transverse Ranges (McCaffrey, 2005). Though these estimates are
716 from kinematic block models using current GPS velocities and do not account for complexities
717 related to comparing long-term and current convergence vectors, such as block rotations. Lastly,
718 salt tectonics can modify the partitioning state and lead to highly complex structures and landforms
719 (e.g., Archer et al., 2012; Lohr et al., 2007).

720 The two natural prototypes that most resemble the models presented here are the Merida Andes
721 of Venezuela and the central Transverse Ranges of the San Andreas fault system (Figure 10b, c).
722 Though these systems are presently exposed to different climatic regimes (San Andreas – semi-
723 Arid; Merida Andes – tropical), we focus mainly on the general results of our experiments because
724 of other confounding variables present in natural systems (lithological heterogeneity, climatic
725 gradients, preexisting structures). These transpressional ranges predominantly exhibit the
726 bivergent wedge structure bounding an uplifted zone of internally deformed topography that we
727 observe in our models.

728 The Merida Andes (Figure 10b) is a roughly 350 km long \times 100 km wide dextral
729 transpressional mountain range that is thought to have begun significant deformation in the Late
730 Miocene (Audemard, 1992; Colletta et al., 1997; Stephan, 1982). Strike-slip deformation is highly
731 partitioned to the Bocono fault, a 500 km dextral strike-slip system, since 15 ± 2 Ma with slip rates
732 of 7.3 – 10.7 mm/a (Audemard, 2003). River systems in the Merida Andes exhibit similar patterns
733 as those described in the laboratory models, including irregular or rectangular drainages, prevalent
734 wind gaps, beheaded or diverted rivers, and densely dissected fault scarps (Audemard, 1999).
735 River channels exhibit deep incision with valley walls as high as 200 – 300 m (Audemard &
736 Audemard, 2002). The high incision and active drainage reorganization result from the highly
737 erosive setting with around 200 cm of yearly rainfall (Martin et al., 2020). The main valley cutting
738 through the Merida Andes follows the trace of the Bocono fault, as we observe in the high erosion
739 model. Considering the exhumation estimates derived from our models, the trace of the Bocono
740 fault, especially in the center of the orogen, should also correspond to the highest amounts of
741 exhumation. Furthermore, the jog in the Bocono fault is appropriately aligned with the ideal *R*-
742 shear orientation and is likely influenced by pre-existing *R*-shear structures. At the tips of the
743 Bocono fault, large alluvial fans reflect its role in sediment routing from the internal portion of the
744 orogen. The \sim 160 km long by \sim 40 km wide triangular feature visible in the northwestern part of

745 the Merida Andes is likely formed by the intersection of the master fault with *R* and *P* shear
746 structures. These similarities with model results suggest that the Merida Andes is in stage 4 (Figure
747 9) of the development of the transpressional system. At this point, deformation and exhumation
748 may be localized to the Bocono fault system by the stream fault feedback. Additionally, pull-apart
749 basins along this structure (Audemard and Audemard, 2002) express the concentrated extension
750 we note in erosion model $\hat{\epsilon}_m$ maps. Projecting into the future, we expect the rhomboidal landforms
751 cut by the Bocono fault to offset left-laterally, as in Figure 9e.

752 The central Transverse Ranges of the San Andreas fault system (Figure 10c) are composed of
753 two distinct lenticular mountain ranges, the San Gabriel and San Bernadino mountains, separated
754 by the main strand of the San Andreas fault. Both mountain ranges are roughly 35 km wide and
755 100 km long. Beginning with the activation of the San Gabriel fault around 12 Ma, which presently
756 bounds the San Gabriel mountains to the south, the transverse ranges were uplifted to elevations
757 > 2000 m and vastly reconfigured. The San Bernadino block was translated as much as 200 km to
758 the southwest by motion along the main San Andreas fault strand starting as early as 5 Ma (Blythe
759 et al., 2002; Matti & Morton, 1993). The evolution of the Transverse ranges strongly resembles
760 the presented model for the topographic and deformational development of transpressional wedges
761 with the present configuration beyond stage 4 (Figure 9e). However, slight differences include
762 more radial drainage patterns around the uplifted San Gabriel and San Bernadino blocks, which
763 are instead bounded by the master fault (San Andreas) and a single wedge-bounding thrust (Figure
764 10c). These variations may relate to the structural and drainage evolution characteristics specific
765 to local transpression along a restraining bend rather than a more continuous continental transform.

766 Considering model observations, valleys corresponding to the master fault system should be
767 the locus of exhumation in transpressional ranges (Figure 8). Where erosion/denudation estimates
768 are available, the presented natural prototypes support this claim. In the central Transverse ranges
769 (Figure 10c), low-temperature thermochronometric ages (Buscher & Spotila, 2007) and
770 denudation rates from radionuclide dating (Binnie et al., 2008) support the hypothesized trends
771 with erosion/denudation rates increasing toward the main San Andreas fault strand. The same
772 trends are apparent further to the northwest in the San Emigdio and Mount Pinos regions, where
773 the western Transverse ranges accommodate most transpressional deformation. There, a low-
774 temperature north-south thermochronometric transect shows a substantial decrease in
775 thermochronometric dates from 19.4 ± 2.4 Ma to 4.4 ± 0.7 Ma across ~ 10 km. The youngest dates
776 are at higher elevations than the older dates within a hanging stream valley, similar to that observed
777 in our models (Niemi et al., 2013). Though, as discussed by Niemi et al., these differences may be
778 partially related to rheological heterogeneity across the San Andreas Fault, which may also apply
779 to the central Transverse Ranges. In the Merida Andes (Figure 10a), though only higher
780 temperature $^{40}\text{Ar}/^{39}\text{Ar}$ thermochronometric data are available, the youngest Muscovite dates
781 (approximately 135 ... 200 Ma) lie along the Bocono fault on the edges of the Chama valley near
782 the city of Mérida. Muscovite $^{40}\text{Ar}/^{39}\text{Ar}$ dates are older outside this valley at ~ 250 ... 425 Ma (van
783 der Lelij et al., 2016). Cosmogenic radionuclide dating (Ott et al., 2023) and low-temperature
784 thermochronology (Pérez-Consuegra et al., 2022) from the central and western Colombian Andes
785 (Figure 10c) show the highest erosion/denudation rates in the lofted Cauca valley (1 km elevation)
786 along the Romeral-Cauca fault systems. Though perhaps coincidentally, we note that the trend of
787 the main valley in each natural prototype supports the observed differences between the final
788 configurations of the presented high and low erosion models. In the more arid central Transverse
789 Ranges, the wedge and main valley trends are dissimilar. Meanwhile, in the wetter central-western

790 Colombian Andes and Merida Andes, the main valley–master fault feature is subparallel to the
791 wedge trend.

792 **5 Conclusions**

793 Erosion plays a significant role in the morphostructural evolution of transpressional systems.
794 High erosion models are characterized by more rectangular drainages and the earlier appearance
795 of low-angle (*Y*- and *P*-shear) structures. In the final stage, a highly partitioned master fault and
796 velocity discontinuity parallel axial valley form. Conversely, low erosion models have drainage
797 networks in the form of deflected fans. Their structural evolution progresses more slowly with the
798 protracted formation of a fully partitioned shear zone. Morphologically, major valleys in the wedge
799 instead follow the traces of synthetic *R*-shears. We propose that these differences result from
800 feedback between stream and fault network development. With more erosion, this feedback is
801 augmented as drainages rearrange more vigorously and incise incipient and actively evolving
802 structures. Mass removal by incision leads to an adjustment in wedge stresses and accelerated
803 structural reconfigurations, which accommodate greater portions of the wrench component of
804 deformation.

805 The results of our experiments assist in understanding patterns of uplift and exhumation in
806 natural transpressional systems. The proposed feedbacks between incision and strike-slip strain
807 localization suggest that, in nature, deeply incised valleys should form along the master fault. The
808 location of this valley is influenced by the concentration of erosion energy due to crustal
809 weakening along fault strike. Maximum exhumation occurs along the wedge axis, which roughly
810 aligns with the velocity discontinuity. Therefore, in natural systems, neglecting confounding
811 variables, including lithology, and pre-existing structure, the intersection of the velocity
812 discontinuity with the throughgoing master fault–main valley feature should yield the highest
813 exhumation rates. The Merida Andes, Transverse Ranges, and central-western Colombian Andes
814 each show patterns demonstrating this trend.

815 We infer that fault and drainage network development are linked to deformation and
816 exhumation patterns in a transpressional system. However, work is needed to fully understand the
817 complexities of the stream-fault feedback. Numerical models that pair the thermomechanical
818 evolution of the wedge with surface processes would be beneficial to clarify the physics of the
819 system and more deeply explore some of the interactions. Additional tectonic-geomorphic field
820 studies focused on continental transpressional systems could provide the data necessary to interpret
821 model results more rigorously in the context of natural systems. Despite the work still to be done,
822 the results of this study provide insight into the range of possible questions, complexities, and
823 future research directions related to the dynamic interactions between processes at the surface and
824 at depth.

825 **Acknowledgments**

826 The authors thank F. Funicello and F. Corbi for coordinating the laboratory component of this
827 work and granting open access to the LET lab at Roma TRE. At Roma TRE, our interpretations of
828 lab results were enhanced through discussions with R. Lanari, R. Clementucci, P. Ballato, and G.
829 Schmidt. The authors also thank the GFZ Helmholtz Centre Potsdam for hosting E. Conrad as a
830 visiting researcher during the Summer of 2022. During this time, the manuscript was greatly
831 improved by discussions with researchers at GFZ, including O. Onken, E. Kosari, and M. Rosenau.
832 This visiting scholarship was funded by the German Academic Exchange Service (DAAD) short-

833 term research grant program. TWB was partially supported by NSF EAR 1927216 and 1925939.
834 CF was partially supported by Dipartimento di Eccellenza grant from Ministero dell'Istruzione e
835 del Merito and from PRIN 2017-2022.

836 **Open Research**

837 Digital elevation models, images used for particle image velocimetry analysis, and grid files of
838 velocity field are available for download from the Texas Data Repository (Conrad, 2023)

839 **References**

- 840 Archer, S. G., Alsop, G. I., Hartley, A. J., Grant, N. T., & Hodgkinson, R. (2012). Salt tectonics,
841 sediments and prospectivity: an introduction. *Geological Society, London, Special*
842 *Publications*, 363(1), 1–6. <https://doi.org/10.1144/SP363.1>
- 843 Audemard, F. (1999). Morpho-Structural Expression of Active Thrust Fault Systems in the
844 Humid Tropical Foothills of Colombia and Venezuela. *Zeitschrift Für Geomorphologie*,
845 118, 1–18.
- 846 Audemard, F. E., & Audemard, F. A. (2002). Structure of the Mérida Andes, Venezuela:
847 relations with the South America–Caribbean geodynamic interaction. *Tectonophysics*,
848 345(1–4), 1–26. [https://doi.org/10.1016/S0040-1951\(01\)00218-9](https://doi.org/10.1016/S0040-1951(01)00218-9)
- 849 Audemard, F. M. (1992). *Tectonics of western Venezuela* (Thesis). Rice University. Retrieved
850 from <https://scholarship.rice.edu/handle/1911/16556>
- 851 Audemard M, F. A. (2003). Geomorphic and geologic evidence of ongoing uplift and
852 deformation in the Mérida Andes, Venezuela. *Quaternary International*, 101–102, 43–65.
853 [https://doi.org/10.1016/S1040-6182\(02\)00128-3](https://doi.org/10.1016/S1040-6182(02)00128-3)
- 854 Babault, J., Driessche, J. V. D., & Teixell, A. (2012). Longitudinal to transverse drainage
855 network evolution in the High Atlas (Morocco): The role of tectonics. *Tectonics*, 31(4).
856 <https://doi.org/10.1029/2011TC003015>
- 857 Barcos, L., Díaz-Azpiroz, M., Balanyá, J. C., Expósito, I., Jiménez-Bonilla, A., & Faccenna, C.
858 (2016). Analogue modelling of inclined, brittle–ductile transpression: Testing analytical

- 859 models through natural shear zones (external Betics). *Tectonophysics*, 682, 169–185.
860 <https://doi.org/10.1016/j.tecto.2016.05.021>
- 861 Binnie, S. A., Phillips, W. M., Summerfield, M. A., Fifield, L. K., & Spotila, J. A. (2008).
862 Patterns of denudation through time in the San Bernardino Mountains, California:
863 Implications for early-stage orogenesis. *Earth and Planetary Science Letters*, 276(1), 62–
864 72. <https://doi.org/10.1016/j.epsl.2008.09.008>
- 865 Bishop, P. (1995). Drainage rearrangement by river capture, beheading and diversion. *Progress*
866 *in Physical Geography: Earth and Environment*, 19(4), 449–473.
867 <https://doi.org/10.1177/030913339501900402>
- 868 Bloom, A. L. (1998). *Geomorphology: a systematic analysis of late Cenozoic landforms*.
869 Prentice Hall Upper Saddle River.
- 870 Blythe, A. E., House, M. A., & Spotila, J. A. (2002). Low-temperature thermochronology of the
871 San Gabriel and San Bernardino Mountains, southern California: Constraining structural
872 evolution. In A. Barth, *Contributions to Crustal Evolution of the Southwestern United*
873 *States*. Geological Society of America. <https://doi.org/10.1130/0-8137-2365-5.231>
- 874 Bonnet, C., Malavieille, J., & Mosar, J. (2007). Interactions between tectonics, erosion, and
875 sedimentation during the recent evolution of the Alpine orogen: Analogue modeling
876 insights. *Tectonics*, 26(6). <https://doi.org/10.1029/2006TC002048>
- 877 Bonnet, C., Malavieille, J., & Mosar, J. (2008). Surface processes versus kinematics of thrust
878 belts: impact on rates of erosion, sedimentation, and exhumation – Insights from
879 analogue models. *Bulletin de La Société Géologique de France*, 179(3), 297–314.
880 <https://doi.org/10.2113/gssgfbull.179.3.297>
- 881 Burbank, D. W., & Anderson, R. S. (2011). *Tectonic Geomorphology*. John Wiley & Sons.

- 882 Buscher, J. T., & Spotila, J. A. (2007). Near-field response to transpression along the southern
883 San Andreas fault, based on exhumation of the northern San Gabriel Mountains, southern
884 California. *Tectonics*, 26(5). <https://doi.org/10.1029/2006TC002017>
- 885 Casas, A. M., Gapais, D., Nalpas, T., Besnard, K., & Román-Berdiel, T. (2001). Analogue
886 models of transpressive systems. *Journal of Structural Geology*, 23(5), 733–743.
887 [https://doi.org/10.1016/S0191-8141\(00\)00153-X](https://doi.org/10.1016/S0191-8141(00)00153-X)
- 888 Castellort, S., Goren, L., Willett, S. D., Champagnac, J.-D., Herman, F., & Braun, J. (2012).
889 River drainage patterns in the New Zealand Alps primarily controlled by plate tectonic
890 strain. *Nature Geoscience*, 5(10), 744–748. <https://doi.org/10.1038/ngeo1582>
- 891 Chorley, R. J., Schumm, S. A., & Sugden, D. E. (1984). *Geomorphology*. London: Routledge.
892 <https://doi.org/10.4324/9780429273636>
- 893 Cloos, H. (1928). Experimente zur inneren tektonik: Centralblatt für Mineralogie, Abt. B.
- 894 Cochran, W. J., Spotila, J. A., Prince, P. S., & McAleer, R. J. (2017). Rapid exhumation of
895 Cretaceous arc-rocks along the Blue Mountains restraining bend of the Enriquillo-
896 Plantain Garden fault, Jamaica, using thermochronometry from multiple closure systems.
897 *Tectonophysics*, 721, 292–309. <https://doi.org/10.1016/j.tecto.2017.09.021>
- 898 Colletta, B., Roure, F., de Toni, B., Loureiro, D., Passalacqua, H., & Gou, Y. (1997). Tectonic
899 inheritance, crustal architecture, and contrasting structural styles in the Venezuela Andes.
900 *Tectonics*, 16(5), 777–794. <https://doi.org/10.1029/97TC01659>
- 901 Conrad, E. (2023). Data for: “Morpho-tectonics of Transpressional Systems: insights from
902 analog modeling” [Dataset]. Texas Data Repository.
903 <https://doi.org/10.18738/T8/5ZKWPI>

- 904 Cooke, M. L., Toeneboehn, K., & Hatch, J. L. (2020). Onset of slip partitioning under oblique
905 convergence within scaled physical experiments. *Geosphere*, *16*(3), 875–889.
906 <https://doi.org/10.1130/GES02179.1>
- 907 Cortés, M., Angelier, J., & Colletta, B. (2005). Paleostress evolution of the northern Andes
908 (Eastern Cordillera of Colombia): Implications on plate kinematics of the South
909 Caribbean region. *Tectonics*, *24*(1). <https://doi.org/10.1029/2003TC001551>
- 910 Cruz, L., Fayon, A., Teyssier, C., & Weber, J. (2007). Exhumation and deformation processes in
911 transpressional orogens: The Venezuelan Paria Península, SE Caribbean–South American
912 plate boundary. In *Special Paper 434: Exhumation Associated with Continental Strike-
913 Slip Fault Systems* (Vol. 434, pp. 149–165). Geological Society of America.
914 [https://doi.org/10.1130/2007.2434\(08\)](https://doi.org/10.1130/2007.2434(08))
- 915 Dahlen, F. A. (1990). Critical Taper Model of Fold-and-Thrust Belts and Accretionary Wedges.
916 *Annual Review of Earth and Planetary Sciences*, *18*(1), 55–99.
917 <https://doi.org/10.1146/annurev.ea.18.050190.000415>
- 918 Dahlen, F. A., & Suppe, J. (1988). Mechanics, growth, and erosion of mountain belts. In
919 *Geological Society of America Special Papers* (Vol. 218, pp. 161–178). Geological
920 Society of America. <https://doi.org/10.1130/SPE218-p161>
- 921 Erikson, J. P., Kelley, S. A., Osmolovsky, P., & Verosub, K. L. (2012). Linked basin
922 sedimentation and orogenic uplift: The Neogene Barinas basin sediments derived from
923 the Venezuelan Andes. *Journal of South American Earth Sciences*, *39*, 138–156.
924 <https://doi.org/10.1016/j.jsames.2012.04.002>

- 925 Fick, S. E., & Hijmans, R. J. (2017). WorldClim 2: new 1-km spatial resolution climate surfaces
926 for global land areas. *International Journal of Climatology*, 37(12), 4302–4315.
927 <https://doi.org/10.1002/joc.5086>
- 928 Fillon, C., Huisman, R. S., & van der Beek, P. (2013). Syntectonic sedimentation effects on the
929 growth of fold-and-thrust belts. *Geology*, 41(1), 83–86. <https://doi.org/10.1130/G33531.1>
- 930 Goren, L., Castelltort, S., & Klinger, Y. (2015). Modes and rates of horizontal deformation from
931 rotated river basins: Application to the Dead Sea fault system in Lebanon. *Geology*,
932 43(9), 843–846. <https://doi.org/10.1130/G36841.1>
- 933 Granger, D. E. (2007). COSMOGENIC NUCLIDE DATING | Landscape Evolution. In S. A.
934 Elias (Ed.), *Encyclopedia of Quaternary Science* (pp. 445–452). Oxford: Elsevier.
935 <https://doi.org/10.1016/B0-44-452747-8/00386-0>
- 936 Gravelleau, F., Hurtrez, J.-E., Dominguez, S., & Malavieille, J. (2011). A new experimental
937 material for modeling relief dynamics and interactions between tectonics and surface
938 processes. *Tectonophysics*, 513(1–4), 68–87. <https://doi.org/10.1016/j.tecto.2011.09.029>
- 939 Gravelleau, Fabien, & Dominguez, S. (2008). Analogue modelling of the interaction between
940 tectonics, erosion and sedimentation in foreland thrust belts. *Comptes Rendus*
941 *Geoscience*, 340(5), 324–333. <https://doi.org/10.1016/j.crte.2008.01.005>
- 942 Gravelleau, Fabien, Malavieille, J., & Dominguez, S. (2012). Experimental modelling of orogenic
943 wedges: A review. *Tectonophysics*, 538–540, 1–66.
944 <https://doi.org/10.1016/j.tecto.2012.01.027>
- 945 Gravelleau, Fabien, Strak, V., Dominguez, S., Malavieille, J., Chatton, M., Manighetti, I., & Petit,
946 C. (2015). Experimental modelling of tectonics–erosion–sedimentation interactions in

- 947 compressional, extensional, and strike–slip settings. *Geomorphology*, 244, 146–168.
948 <https://doi.org/10.1016/j.geomorph.2015.02.011>
- 949 Guerit, L., Dominguez, S., Malavieille, J., & Castelltort, S. (2016). Deformation of an
950 experimental drainage network in oblique collision. *Tectonophysics*, 693, 210–222.
951 <https://doi.org/10.1016/j.tecto.2016.04.016>
- 952 Guerit, Laure, Goren, L., Dominguez, S., Malavieille, J., & Castelltort, S. (2018). Landscape
953 ‘stress’ and reorganization from χ -maps: Insights from experimental drainage networks in
954 oblique collision setting. *Earth Surface Processes and Landforms*, 43(15), 3152–3163.
955 <https://doi.org/10.1002/esp.4477>
- 956 Hallet, B., & Molnar, P. (2001). Distorted drainage basins as markers of crustal strain east of the
957 Himalaya. *Journal of Geophysical Research: Solid Earth*, 106(B7), 13697–13709.
958 <https://doi.org/10.1029/2000JB900335>
- 959 Hecht, H., & Oguchi, T. (2017). Global evaluation of erosion rates in relation to tectonics.
960 *Progress in Earth and Planetary Science*, 4(1), 40. [https://doi.org/10.1186/s40645-017-](https://doi.org/10.1186/s40645-017-0156-3)
961 0156-3
- 962 Hilley, G. E., & Strecker, M. R. (2004). Steady state erosion of critical Coulomb wedges with
963 applications to Taiwan and the Himalaya. *Journal of Geophysical Research: Solid Earth*,
964 109(B1). <https://doi.org/10.1029/2002JB002284>
- 965 Hubbert, M. K. (1937). Theory of scale models as applied to the study of geologic structures.
966 *GSA Bulletin*, 48(10), 1459–1520. <https://doi.org/10.1130/GSAB-48-1459>
- 967 Hubbert, M. K. (1951). MECHANICAL BASIS FOR CERTAIN FAMILIAR GEOLOGIC
968 STRUCTURES. *GSA Bulletin*, 62(4), 355–372. [https://doi.org/10.1130/0016-](https://doi.org/10.1130/0016-7606(1951)62[355:MBFCFG]2.0.CO;2)
969 7606(1951)62[355:MBFCFG]2.0.CO;2

- 970 Keller, J. V. A., Hall, S. H., & McClay, K. R. (1997). Shear fracture pattern and microstructural
971 evolution in transpressional fault zones from field and laboratory studies. *Journal of*
972 *Structural Geology*, 19(9), 1173–1187. [https://doi.org/10.1016/S0191-8141\(97\)00042-4](https://doi.org/10.1016/S0191-8141(97)00042-4)
- 973 Konstantinovskaia, E., & Malavieille, J. (2005). Erosion and exhumation in accretionary
974 orogens: Experimental and geological approaches. *Geochemistry, Geophysics,*
975 *Geosystems*, 6(2). <https://doi.org/10.1029/2004GC000794>
- 976 Koons, P. O. (1995). Modeling the Topographic Evolution of Collisional Belts. *Annual Review*
977 *of Earth and Planetary Sciences*, 23(1), 375–408.
978 <https://doi.org/10.1146/annurev.ea.23.050195.002111>
- 979 Koons, Peter O. (1994). Three-dimensional critical wedges: Tectonics and topography in oblique
980 collisional orogens. *Journal of Geophysical Research: Solid Earth*, 99(B6), 12301–
981 12315. <https://doi.org/10.1029/94JB00611>
- 982 Lague, D., Crave, A., & Davy, P. (2003). Laboratory experiments simulating the geomorphic
983 response to tectonic uplift. *Journal of Geophysical Research: Solid Earth*, 108(B1), ETG
984 3-1-ETG 3-20. <https://doi.org/10.1029/2002JB001785>
- 985 Lallemand, S. E., Schnürle, P., & Malavieille, J. (1994). Coulomb theory applied to accretionary
986 and nonaccretionary wedges: Possible causes for tectonic erosion and/or frontal
987 accretion. *Journal of Geophysical Research: Solid Earth*, 99(B6), 12033–12055.
988 <https://doi.org/10.1029/94JB00124>
- 989 Leever, K. A., Gabrielsen, R. H., Faleide, J. I., & Braathen, A. (2011). A transpressional origin
990 for the West Spitsbergen fold-and-thrust belt: Insight from analog modeling. *Tectonics*,
991 30(2). <https://doi.org/10.1029/2010TC002753>

- 992 Leever, K. A., Gabrielsen, R. H., Sokoutis, D., & Willingshofer, E. (2011). The effect of
993 convergence angle on the kinematic evolution of strain partitioning in transpressional
994 brittle wedges: Insight from analog modeling and high-resolution digital image analysis:
995 KINEMATICS OF STRAIN PARTITIONING. *Tectonics*, 30(2), n/a-n/a.
996 <https://doi.org/10.1029/2010TC002823>
- 997 van der Lelij, R., Spikings, R., & Mora, A. (2016). Thermochemistry and tectonics of the
998 Mérida Andes and the Santander Massif, NW South America. *Lithos*, 248–251, 220–239.
999 <https://doi.org/10.1016/j.lithos.2016.01.006>
- 1000 Leopold, L. B., & Bull, W. B. (1979). Base Level, Aggradation, and Grade. *Proceedings of the*
1001 *American Philosophical Society*, 123(3), 168–202.
- 1002 Liu, Y., Tan, X., Ye, Y., Zhou, C., Lu, R., Murphy, M. A., et al. (2020). Role of erosion in
1003 creating thrust recesses in a critical-taper wedge: An example from Eastern Tibet. *Earth*
1004 *and Planetary Science Letters*, 540, 116270. <https://doi.org/10.1016/j.epsl.2020.116270>
- 1005 Lohr, T., Krawczyk, C. M., Tanner, D. C., Samiee, R., Endres, H., Oncken, O., et al. (2007).
1006 Strain partitioning due to salt: insights from interpretation of a 3D seismic data set in the
1007 NW German Basin. *Basin Research*, 19(4), 579–597. [https://doi.org/10.1111/j.1365-](https://doi.org/10.1111/j.1365-2117.2007.00338.x)
1008 [2117.2007.00338.x](https://doi.org/10.1111/j.1365-2117.2007.00338.x)
- 1009 Malavieille, J., Larroque, C., & Calassou, S. (1993). Experimental modelling of
1010 tectonic/sedimentation relationships between forearc basin and accretionary wedge.
1011 *COMPTES RENDUS-ACADEMIE DES SCIENCES PARIS SERIE 2*, 316, 1131–1131.
- 1012 Malavieille, Jacques. (2010). Impact of erosion, sedimentation, and structural heritage on the
1013 structure and kinematics of orogenic wedges: Analog models and case studies. *GSA*
1014 *Today*, 4–10. <https://doi.org/10.1130/GSATG48A.1>

- 1015 Malavieille, Jacques, Dominguez, S., Lu, C.-Y., Chen, C.-T., & Konstantinovskaya, E. (2021).
1016 Deformation partitioning in mountain belts: insights from analogue modelling
1017 experiments and the Taiwan collisional orogen. *Geological Magazine*, 158(1), 84–103.
1018 <https://doi.org/10.1017/S0016756819000645>
- 1019 Mao, Y., Li, Y., Yan, B., Wang, X., Jia, D., & Chen, Y. (2021). Response of Surface Erosion to
1020 Crustal Shortening and its Influence on Tectonic Evolution in Fold-and-Thrust Belts:
1021 Implications From Sandbox Modeling on Tectonic Geomorphology. *Tectonics*, 40(5),
1022 e2020TC006515. <https://doi.org/10.1029/2020TC006515>
- 1023 Marshak, S. (2004). Salients, Recesses, Arcs, Oroclines, and Syntaxes A Review of Ideas
1024 Concerning the Formation of Map-view Curves in Fold-thrust Belts, 131–156.
- 1025 Martin, L. C. P., Blard, P.-H., Lavé, J., Jomelli, V., Charreau, J., Condom, T., et al. (2020).
1026 Antarctic-like temperature variations in the Tropical Andes recorded by glaciers and
1027 lakes during the last deglaciation. *Quaternary Science Reviews*, 247, 106542.
1028 <https://doi.org/10.1016/j.quascirev.2020.106542>
- 1029 Matti, J. C., & Morton, D. M. (1993). Chapter 2: Paleogeographic evolution of the San Andreas
1030 fault in southern California: A reconstruction based on a new cross-fault correlation. In
1031 *Geological Society of America Memoirs* (Vol. 178, pp. 107–160). Geological Society of
1032 America. <https://doi.org/10.1130/MEM178-p107>
- 1033 McCaffrey, R. (2005). Block kinematics of the Pacific–North America plate boundary in the
1034 southwestern United States from inversion of GPS, seismological, and geologic data.
1035 *Journal of Geophysical Research: Solid Earth*, 110(B7).
1036 <https://doi.org/10.1029/2004JB003307>

- 1037 Molnar, P., & England, P. (1990). Late Cenozoic uplift of mountain ranges and global climate
1038 change: chicken or egg? *Nature*, *346*(6279), 29–34. <https://doi.org/10.1038/346029a0>
- 1039 Mora-Páez, H., Kellogg, J. N., Freymueller, J. T., Mencin, D., Fernandes, R. M. S., Diederix, H.,
1040 et al. (2019). Crustal deformation in the northern Andes – A new GPS velocity field.
1041 *Journal of South American Earth Sciences*, *89*, 76–91.
1042 <https://doi.org/10.1016/j.jsames.2018.11.002>
- 1043 Naylor, M. A., Mandl, G., & Supesteijn, C. H. K. (1986). Fault geometries in basement-induced
1044 wrench faulting under different initial stress states. *Journal of Structural Geology*, *8*(7),
1045 737–752. [https://doi.org/10.1016/0191-8141\(86\)90022-2](https://doi.org/10.1016/0191-8141(86)90022-2)
- 1046 Niemi, N. A., Buscher, J. T., Spotila, J. A., House, M. A., & Kelley, S. A. (2013). Insights from
1047 low-temperature thermochronometry into transpressional deformation and crustal
1048 exhumation along the San Andreas fault in the western Transverse Ranges, California.
1049 *Tectonics*, *32*(6), 1602–1622. <https://doi.org/10.1002/2013TC003377>
- 1050 Ott, R. F., Gallen, S. F., & Helman, D. (2023). *Erosion and weathering in carbonate regions*
1051 *reveal climatic and tectonic drivers of carbonate landscape evolution* (preprint).
1052 Physical: Landscape Evolution: modelling and field studies.
1053 <https://doi.org/10.5194/egusphere-2022-1376>
- 1054 Paola, C., Straub, K., Mohrig, D., & Reinhardt, L. (2009). The “unreasonable effectiveness” of
1055 stratigraphic and geomorphic experiments. *Earth-Science Reviews*, *97*(1–4), 1–43.
1056 <https://doi.org/10.1016/j.earscirev.2009.05.003>
- 1057 Peakall, J., Ashworth, P., & Best, J. (1996). *Physical Modelling in Fluvial Geomorphology:*
1058 *Principles, Applications and Unresolved Issues* (pp. 221–253).

- 1059 Pérez-Consuegra, N., Hoke, G. D., Fitzgerald, P., Mora, A., Sobel, E. R., & Glodny, J. (2022).
1060 Late Miocene–Pliocene onset of fluvial incision of the Cauca River Canyon in the
1061 Northern Andes. *GSA Bulletin*, *134*(9–10), 2453–2468. <https://doi.org/10.1130/B36047.1>
- 1062 Perrin, C., Clemenzi, L., Malavieille, J., Molli, G., Taboada, A., & Dominguez, S. (2013).
1063 Impact of erosion and décollements on large-scale faulting and folding in orogenic
1064 wedges: analogue models and case studies. *Journal of the Geological Society*, *170*(6),
1065 893–904. <https://doi.org/10.1144/jgs2013-012>
- 1066 Philippon, M., & Corti, G. (2016). Obliquity along plate boundaries. *Tectonophysics*, *693*, 171–
1067 182. <https://doi.org/10.1016/j.tecto.2016.05.033>
- 1068 Pinet, N., & Cobbold, P. R. (1992). Experimental insights into the partitioning of motion within
1069 zones of oblique subduction. *Tectonophysics*, *206*(3), 371–388.
1070 [https://doi.org/10.1016/0040-1951\(92\)90388-M](https://doi.org/10.1016/0040-1951(92)90388-M)
- 1071 Raffel, M., Willert, C., Wereley, S., & Kompenhans, J. (2007). *Particle Image Velocimetry - A*
1072 *Practical Guide (2nd Edition)*. Springer Verlag, Berlin, Heidelberg, New York. Retrieved
1073 from <http://www.springer.com>
- 1074 Ramberg, H. (1981). *Gravity, deformation, and the earth's crust: in theory, experiments, and*
1075 *geological application* (2d ed). London: Academic Press. Retrieved from [http://bvbr.bib-](http://bvbr.bib-bvb.de:8991/F?func=service&doc_library=BVB01&local_base=BVB01&doc_number=01368211&line_number=0001&func_code=DB_RECORDS&service_type=MEDIA)
1076 [bvb.de:8991/F?func=service&doc_library=BVB01&local_base=BVB01&doc_number=0](http://bvbr.bib-bvb.de:8991/F?func=service&doc_library=BVB01&local_base=BVB01&doc_number=01368211&line_number=0001&func_code=DB_RECORDS&service_type=MEDIA)
1077 [01368211&line_number=0001&func_code=DB_RECORDS&service_type=MEDIA](http://bvbr.bib-bvb.de:8991/F?func=service&doc_library=BVB01&local_base=BVB01&doc_number=01368211&line_number=0001&func_code=DB_RECORDS&service_type=MEDIA)
- 1078 Ramsey, L. A., Walker, R. T., & Jackson, J. (2007). Geomorphic constraints on the active
1079 tectonics of southern Taiwan. *Geophysical Journal International*, *170*(3), 1357–1372.
1080 <https://doi.org/10.1111/j.1365-246X.2007.03444.x>

- 1081 Reitano, R., Faccenna, C., Funiciello, F., Corbi, F., & Willett, S. D. (2020). Erosional response
1082 of granular material in landscape models. *Earth Surface Dynamics*, 8(4), 973–993.
1083 <https://doi.org/10.5194/esurf-8-973-2020>
- 1084 Reitano, R., Faccenna, C., Funiciello, F., Corbi, F., Sternai, P., Willett, S., et al. (2022).
1085 Sediment Recycling and the Evolution of Analog Orogenic Wedges. *Tectonics*, 41.
1086 <https://doi.org/10.1029/2021TC006951>
- 1087 Reitano, R., Clementucci, R., Conrad, E. M., Corbi, F., Lanari, R., Faccenna, C., & Bazzucchi,
1088 C. (2023). *Stream laws in tectonic landscape analogue models* (preprint). Physical:
1089 Landscape Evolution: modelling and field studies. [https://doi.org/10.5194/egusphere-](https://doi.org/10.5194/egusphere-2022-911)
1090 [2022-911](https://doi.org/10.5194/egusphere-2022-911)
- 1091 Reitman, N. G., Klinger, Y., Briggs, R. W., & Gold, R. D. (2022). Climatic influence on the
1092 expression of strike-slip faulting. *Geology*, 51(1), 18–22.
1093 <https://doi.org/10.1130/G50393.1>
- 1094 Riedel, W. (1929). Zur Mechanik geologischer Brucherscheinungen. *Centralblatt Für*
1095 *Mineralogie, Geologie Und Paläontologie*, 8, 354–368.
- 1096 Roe, G. H., Stolar, D. B., & Willett, S. D. (2006). Response of a steady-state critical wedge
1097 orogen to changes in climate and tectonic forcing. In Sean D. Willett, N. Hovius, M. T.
1098 Brandon, & D. M. Fisher, *Tectonics, Climate, and Landscape Evolution*. Geological
1099 Society of America. [https://doi.org/10.1130/2005.2398\(13\)](https://doi.org/10.1130/2005.2398(13))
- 1100 Roy, M., & Royden, L. H. (2000a). Crustal rheology and faulting at strike-slip plate boundaries:
1101 1. An analytic model. *Journal of Geophysical Research: Solid Earth*, 105(B3), 5583–
1102 5597. <https://doi.org/10.1029/1999JB900339>

- 1103 Roy, M., & Royden, L. H. (2000b). Crustal rheology and faulting at strike-slip plate boundaries:
1104 2. Effects of lower crustal flow. *Journal of Geophysical Research: Solid Earth*, *105*(B3),
1105 5599–5613. <https://doi.org/10.1029/1999JB900340>
- 1106 Sanderson, D. J., & Marchini, W. R. D. (1984). Transpression. *Journal of Structural Geology*,
1107 *6*(5), 449–458. [https://doi.org/10.1016/0191-8141\(84\)90058-0](https://doi.org/10.1016/0191-8141(84)90058-0)
- 1108 Sapozhnikov, V. B., & Fofoula-Georgiou, E. (1996). Do the Current Landscape Evolution
1109 Models Show Self-Organized Criticality? *Water Resources Research*, *32*(4), 1109–1112.
1110 <https://doi.org/10.1029/96WR00161>
- 1111 Schreurs, G., & Colletta, B. (2002). Analogue modelling of continental transpression. *Journal of*
1112 *the Virtual Explorer*, *07*, 103–114.
- 1113 Schreurs, Guido, & Colletta, B. (1998). Analogue modelling of faulting in zones of continental
1114 transpression and transtension. *Geological Society, London, Special Publications*, *135*(1),
1115 59–79. <https://doi.org/10.1144/GSL.SP.1998.135.01.05>
- 1116 Schwanghart, W., & Scherler, D. (2014). Short Communication: TopoToolbox 2 – MATLAB-
1117 based software for topographic analysis and modeling in Earth surface sciences. *Earth*
1118 *Surface Dynamics*, *2*(1), 1–7. <https://doi.org/10.5194/esurf-2-1-2014>
- 1119 Simpson, G. D. H. (2006). Modelling interactions between fold–thrust belt deformation, foreland
1120 flexure and surface mass transport. *Basin Research*, *18*(2), 125–143.
1121 <https://doi.org/10.1111/j.1365-2117.2006.00287.x>
- 1122 Steer, P., Simoes, M., Cattin, R., & Shyu, J. B. H. (2014). Erosion influences the seismicity of
1123 active thrust faults. *Nature Communications*, *5*(1), 5564.
1124 <https://doi.org/10.1038/ncomms6564>

- 1125 Stephan, J.-F. (1982). *Evolution géodynamique du domaine Caraïbe Andes et chaîne Caraïbe sur*
1126 *la transversale de Barquisimeto (Vénézuéla)* (PhD Thesis). Éditeur inconnu.
- 1127 Stockmal, G. S., Beaumont, C., Nguyen, M., & Lee, B. (2007). Mechanics of thin-skinned fold-
1128 and-thrust belts: Insights from numerical models. In *Special Paper 433: Whence the*
1129 *Mountains? Inquiries into the Evolution of Orogenic Systems: A Volume in Honor of*
1130 *Raymond A. Price* (Vol. 433, pp. 63–98). Geological Society of America.
1131 [https://doi.org/10.1130/2007.2433\(04\)](https://doi.org/10.1130/2007.2433(04))
- 1132 Strak, V., Dominguez, S., Petit, C., Meyer, B., & Loget, N. (2011). Interaction between normal
1133 fault slip and erosion on relief evolution: Insights from experimental modelling.
1134 *Tectonophysics*, 513(1), 1–19. <https://doi.org/10.1016/j.tecto.2011.10.005>
- 1135 Suter, F., Sartori, M., Neuwerth, R., & Gorin, G. (2008). Structural imprints at the front of the
1136 Chocó-Panamá indenter: Field data from the North Cauca Valley Basin, Central
1137 Colombia. *Tectonophysics*, 460(1), 134–157. <https://doi.org/10.1016/j.tecto.2008.07.015>
- 1138 Tchalenko, J. S. (1968). The evolution of kink-bands and the development of compression
1139 textures in sheared clays. *Tectonophysics*, 6(2), 159–174. [https://doi.org/10.1016/0040-](https://doi.org/10.1016/0040-1951(68)90017-6)
1140 [1951\(68\)90017-6](https://doi.org/10.1016/0040-1951(68)90017-6)
- 1141 Tchalenko, J. S. (1970). Similarities between Shear Zones of Different Magnitudes. *GSA*
1142 *Bulletin*, 81(6), 1625–1640. [https://doi.org/10.1130/0016-](https://doi.org/10.1130/0016-7606(1970)81[1625:SBSZOD]2.0.CO;2)
1143 [7606\(1970\)81\[1625:SBSZOD\]2.0.CO;2](https://doi.org/10.1130/0016-7606(1970)81[1625:SBSZOD]2.0.CO;2)
- 1144 Tchalenko, J. S., & Ambraseys, N. N. (1970). Structural Analysis of the Dasht-e Bayaz (Iran)
1145 Earthquake Fractures. *GSA Bulletin*, 81(1), 41–60. [https://doi.org/10.1130/0016-](https://doi.org/10.1130/0016-7606(1970)81[41:SAOTDB]2.0.CO;2)
1146 [7606\(1970\)81\[41:SAOTDB\]2.0.CO;2](https://doi.org/10.1130/0016-7606(1970)81[41:SAOTDB]2.0.CO;2)

- 1147 Teyssier, C., Tikoff, B., & Markley, M. (1995). Oblique plate motion and continental tectonics.
1148 *Geology*, 23(5), 447–450. <https://doi.org/10.1130/0091->
1149 [7613\(1995\)023<0447:OPMACT>2.3.CO;2](https://doi.org/10.1130/0091-7613(1995)023<0447:OPMACT>2.3.CO;2)
- 1150 Thielicke, W., & Sonntag, R. (2021). Particle Image Velocimetry for MATLAB: Accuracy and
1151 enhanced algorithms in PIVlab. *Journal of Open Research Software*, 9(1), 12.
1152 <https://doi.org/10.5334/jors.334>
- 1153 Tikoff, B., & Teyssier, C. (1994). Strain modeling of displacement-field partitioning in
1154 transpressional orogens. *Journal of Structural Geology*, 16(11), 1575–1588.
1155 [https://doi.org/10.1016/0191-8141\(94\)90034-5](https://doi.org/10.1016/0191-8141(94)90034-5)
- 1156 Vermeer, P. A., & De Borst, R. (1984). Non-associated plasticity for soils, concrete and rock.
1157 *HERON*, 29 (3), 1984.
- 1158 Viaplana-Muzas, M., Babault, J., Dominguez, S., Van Den Driessche, J., & Legrand, X. (2015).
1159 Drainage network evolution and patterns of sedimentation in an experimental wedge.
1160 *Tectonophysics*, 664, 109–124. <https://doi.org/10.1016/j.tecto.2015.09.007>
- 1161 Viaplana-Muzas, M., Babault, J., Dominguez, S., Van Den Driessche, J., & Legrand, X. (2019).
1162 Modelling of drainage dynamics influence on sediment routing system in a fold-and-
1163 thrust belt. *Basin Research*, 31(2), 290–310. <https://doi.org/10.1111/bre.12321>
- 1164 Wessel, P., Luis, J. F., Uieda, L., Scharroo, R., Wobbe, F., Smith, W. H. F., & Tian, D. (2019).
1165 The Generic Mapping Tools Version 6. *Geochemistry, Geophysics, Geosystems*, 20(11),
1166 5556–5564. <https://doi.org/10.1029/2019GC008515>
- 1167 Wilcox, R. E., Harding, T. P., & Seely, D. R. (1973). Basic Wrench Tectonics. *AAPG Bulletin*,
1168 57. <https://doi.org/10.1306/819A424A-16C5-11D7-8645000102C1865D>

- 1169 Willett, S. D. (1999). Orogeny and orography: The effects of erosion on the structure of
1170 mountain belts. *Journal of Geophysical Research: Solid Earth*, 104(B12), 28957–28981.
1171 <https://doi.org/10.1029/1999JB900248>
- 1172 Zeitler, P. K., Koons, P. O., Bishop, M. P., Chamberlain, C. P., Craw, D., Edwards, M. A., et al.
1173 (2001). Crustal reworking at Nanga Parbat, Pakistan: Metamorphic consequences of
1174 thermal-mechanical coupling facilitated by erosion. *Tectonics*, 20(5), 712–728.
1175 <https://doi.org/10.1029/2000TC001243>

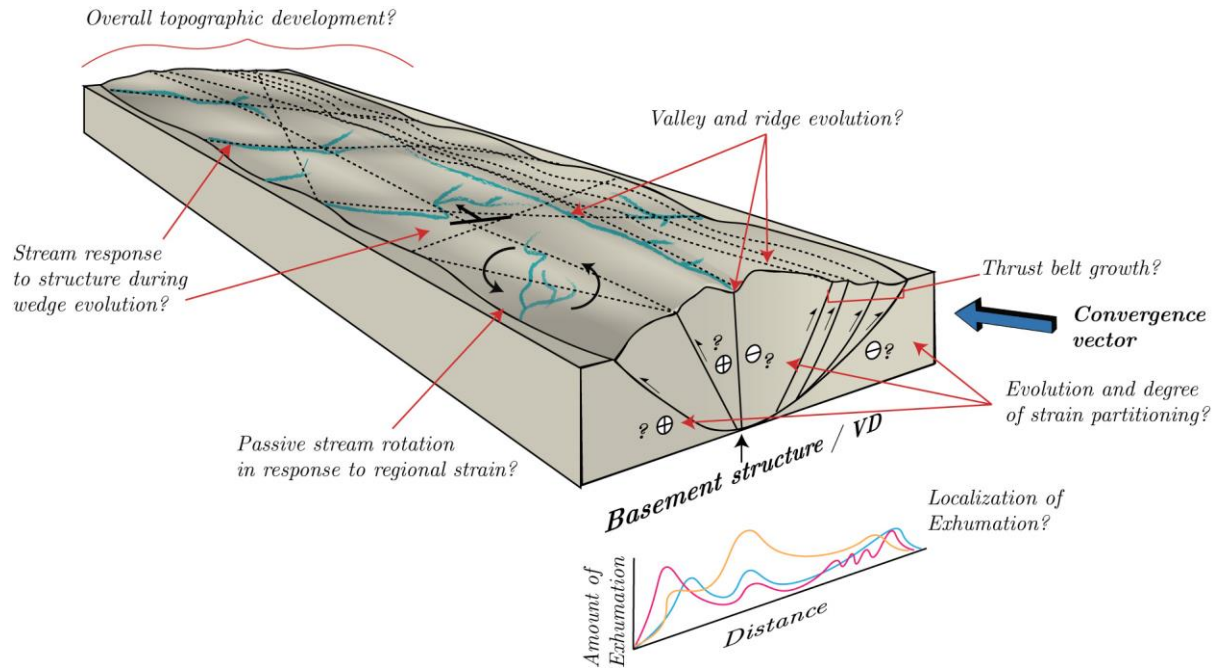


Figure 1. Illustration highlighting the unresolved components of transpressional (left-lateral) wedge growth addressed in this paper. The velocity discontinuity (VD) and convergence vector are in bold font. Dashed lines on topography show fault traces. The x-y plots show hypothetical exhumation patterns (colored lines) across the wedge. Examples of stream responses to structure shown include drainage deflection (black arrow showing offset), headward erosion, and entrainment along faults. Black rotation arrows indicate the direction of rotation in a left-lateral transpressional orogen.

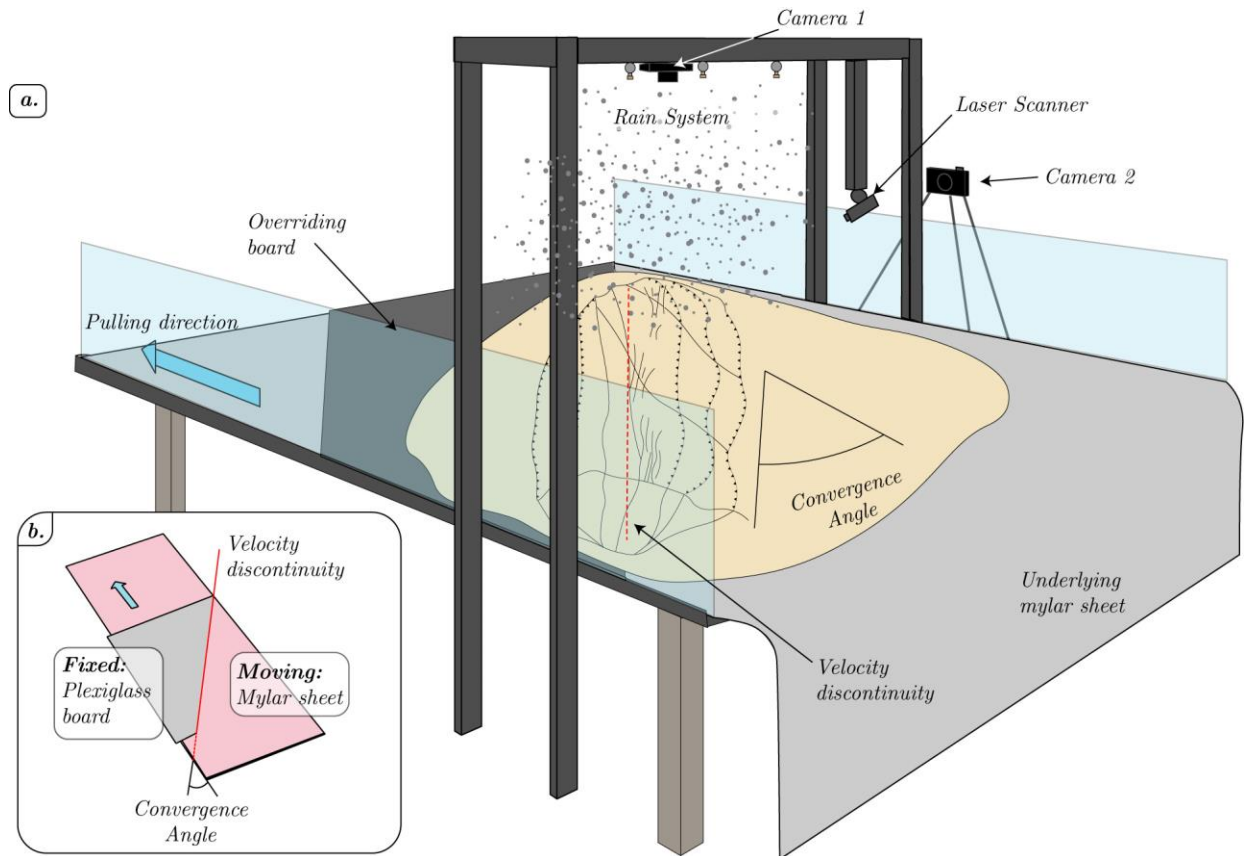


Figure 2. Experimental setup (a) Cartoon showing the full sandbox model set-up. The experiment comprises a $2 \times 1 \times 1$ m plexiglass box set on a tabletop. The beige feature represents the material loaded on top. The red line shows the velocity discontinuity, and the blue arrow on the left is the pulling direction. The motor that pulls the mylar sheet is not pictured. (b) The velocity discontinuity set-up that was put into the box to generate a deformational wedge. The gray color represents the plexiglass board cut to the desired convergence angle ($25 \times 100 \times 60 \times 96 \times 0.2$ cm). The pink represents the mylar sheet that was pulled under the board. The velocity discontinuity (red line) is the interface between the fixed and moving materials.

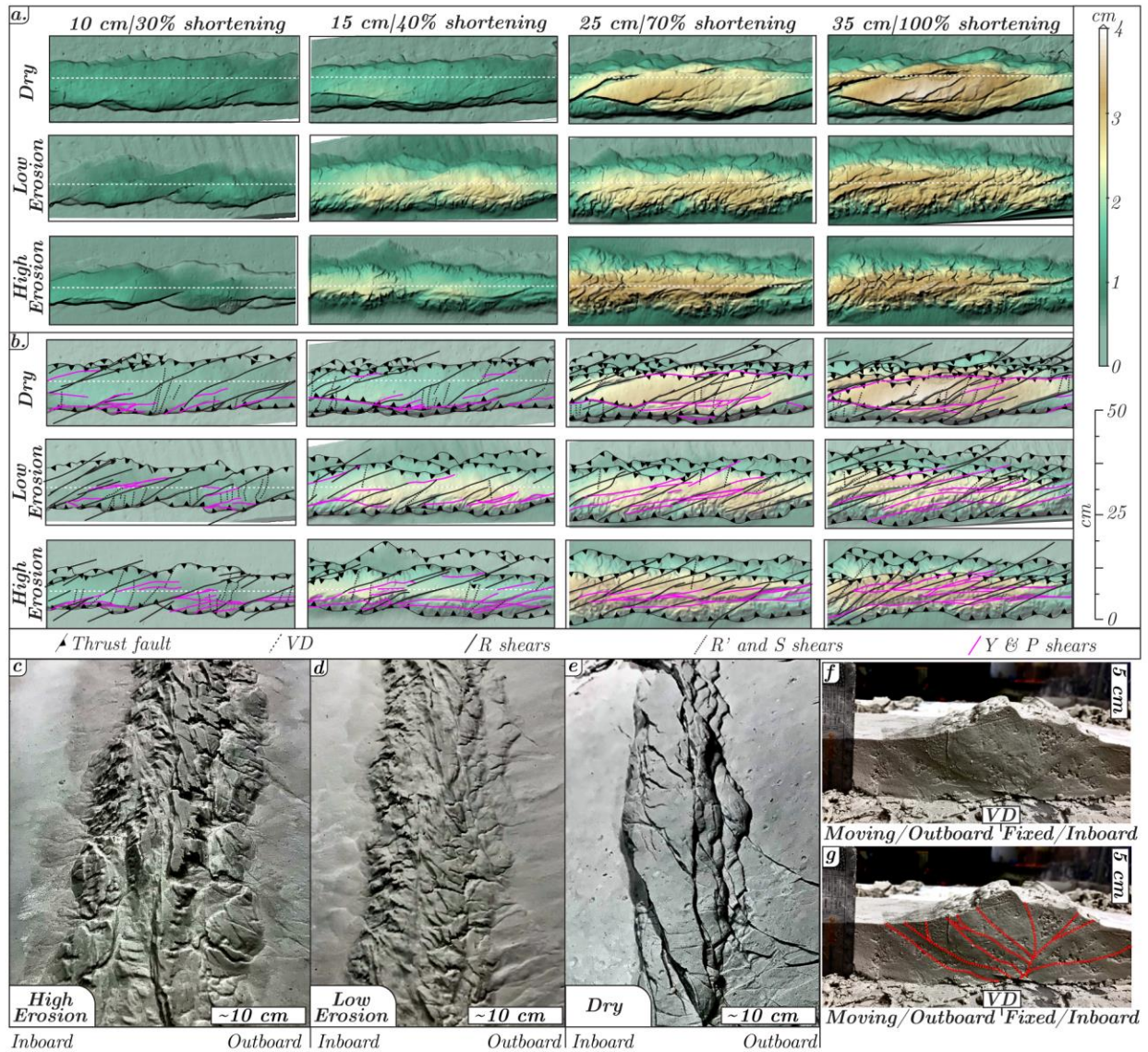


Figure 3. Overview of the results of selected experiments. (a) Digital elevation models (DEMs) across shortening stages. Rows show increasing erosion and columns show increasing convergence/shortening. White lines represent the location of the velocity discontinuity (VD). (b) Interpreted structures showing thrusts (decorated lines), the VD (white dashed line), riedel (*R*) shears (black lines), anti-riedel (*R'*) shears and connecting splay (*S*) faults (dotted black lines), and low-angle faults (*Y* and *P* shears, see text for description, magenta lines). (c-e) Contrast-enhanced oblique images at the final stage of each

model. Scale bars are only accurate at the bottom of the images due to perspective distortion. Note the alluvial fans in the erosion models (c,d). (f-g) Contrast-enhanced images showing the uninterpreted (f) and (g) interpreted cross sections of the high erosion model.

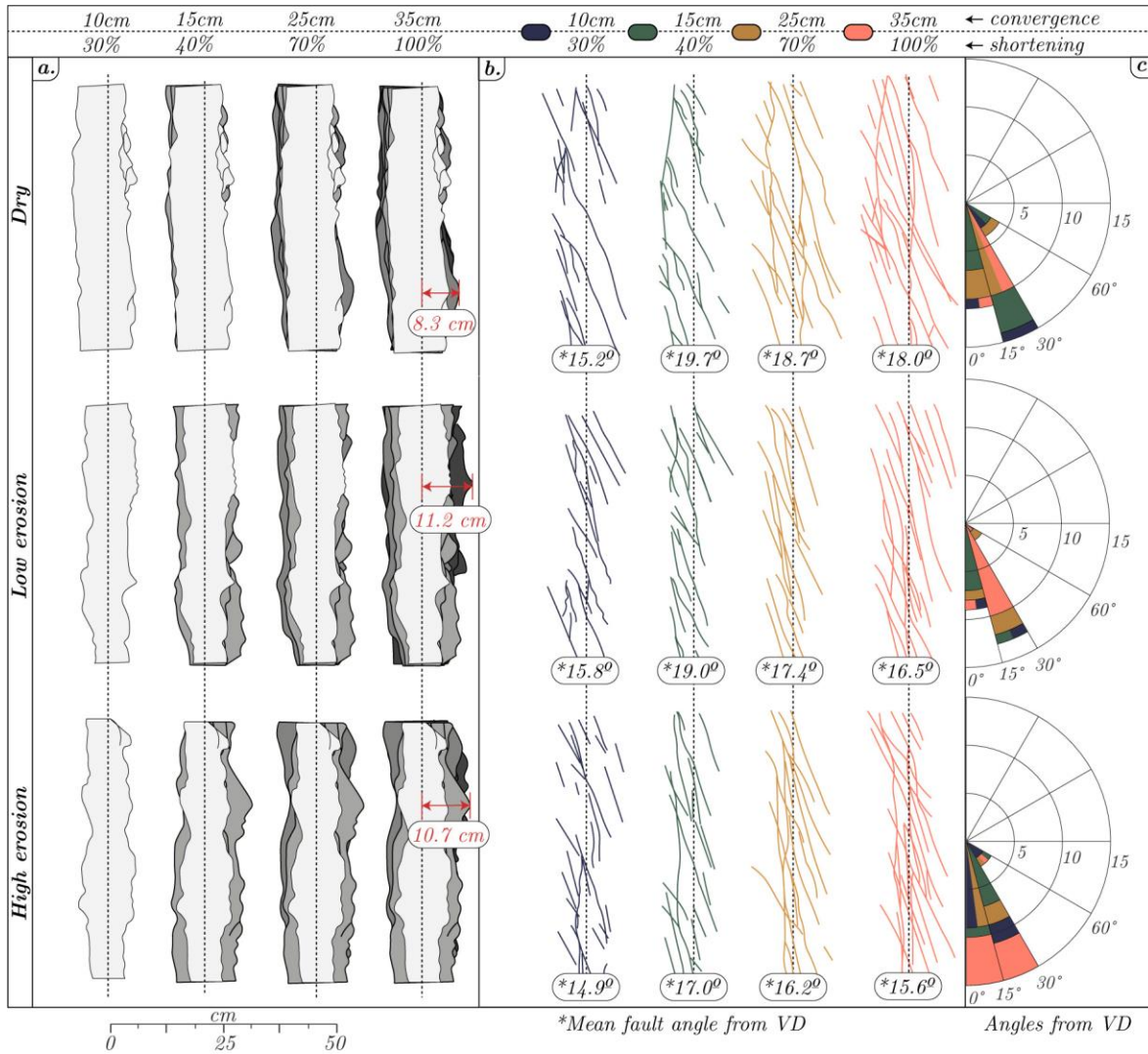


Figure 4. The evolution of thrust sheets and internal strike-slip faults with increasing shortening. The upper, middle, and lower rows show the dry, low erosion, and high erosion models, respectively. (a) Change in thrust belts with increasing convergence. Each grey shade represents a horizontal slice through the wedge. These slices are stacked at each convergence step. The horizontal black dashed lines are the velocity discontinuity. (b) The evolving internal strike-slip structure of the models. (c) Polar histograms showing the number of structures within 15° bins from 0 to 60°. Colors in the histograms correspond to the convergence stages, as shown at the top of the figure. Split bins represent subsequent stages

with no change in count. Faults and fractures $> 60^\circ$ and $< 0^\circ$ were included in the nearest bins because they are uncommon and deviate only small amounts from those angles.

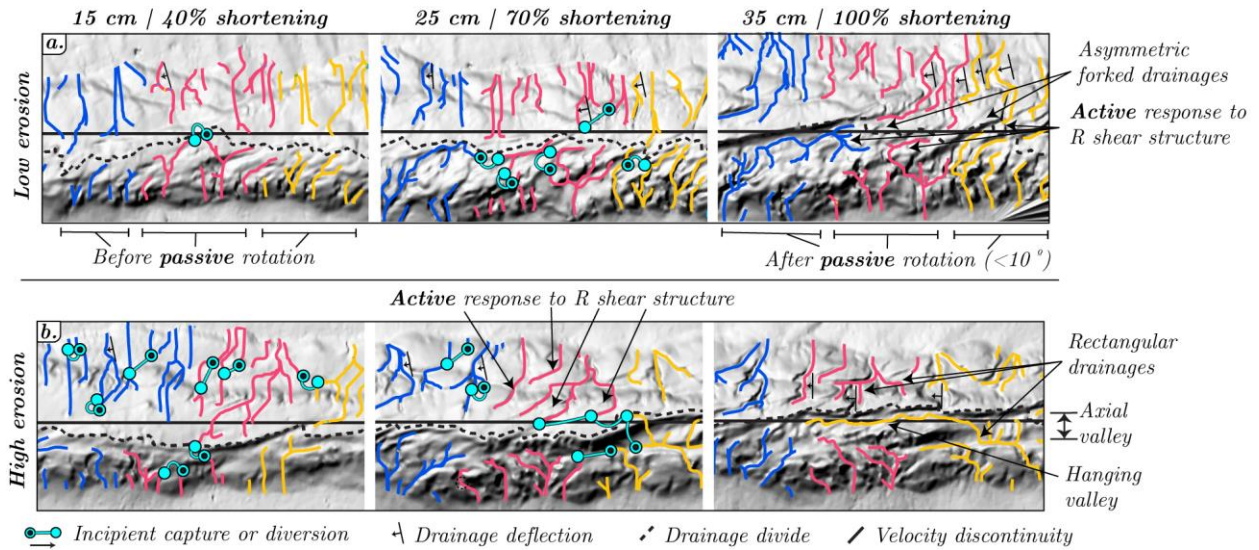


Figure 5. Snapshots of stream evolution between erosion models. Streams are cut to the lowest thrust sheet and colored as a visual aid to tracking reorganization mechanisms between frames. (a) Low erosion model. The active drainage response to structure is more delayed, while the passive rotation is better expressed (preserved). Drainage networks exhibit asymmetric forked patterns in the final stage. (b) High erosion model. The active drainage response to structure occurs earlier, yet there is a less apparent passive rotation response. Final drainage patterns are rectangular in form.

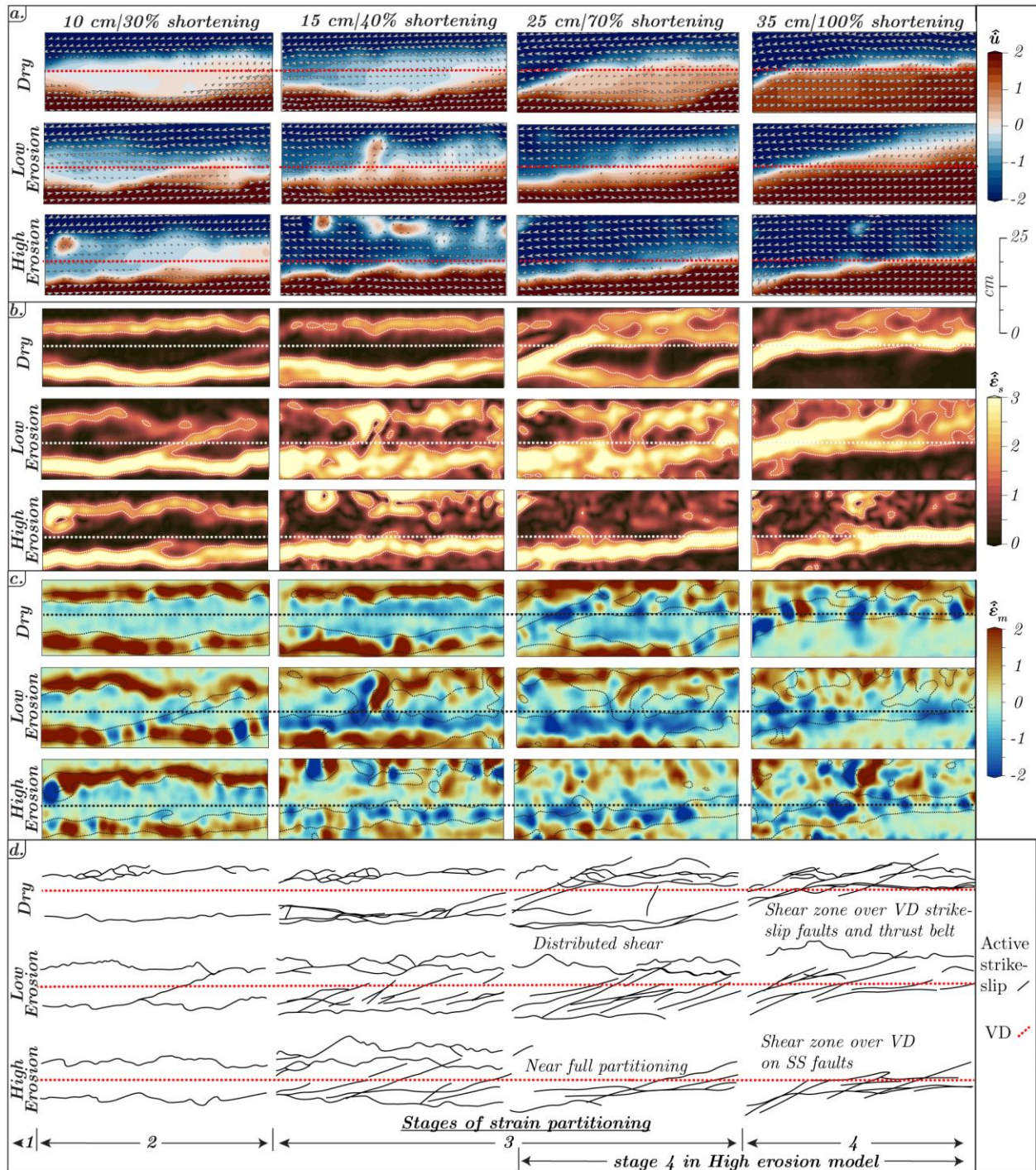


Figure 6. Evolution of strain partitioning from PIV at the same stages shown in Figures 2, 3, and 4. (a) The normalized horizontal velocity components (\hat{u}). Sharp color contrast indicates locations of strike-slip deformation. Irregular red blobs show locations of land sliding or

noise caused by mist interference. The dashed red line indicates the velocity discontinuity (VD). (b) The normalized maximum horizontal shear strain-rate at each stage ($\hat{\epsilon}_s$). White dotted lines are superimposed $\hat{\epsilon}_s = 1.5$ contours. The dashed white line indicates the VD. (c) The normalized dilatational strain-rate, ($\hat{\epsilon}_m$). Positive values (red) indicate compression and negative values (blue) indicate extension. Black dotted lines are superimposed $\hat{\epsilon}_s = 1.5$ contours. The dashed black line indicates the VD. (d) Active faults are determined by interpreting fault locations with respect to \hat{u} and $\hat{\epsilon}_s$. The dashed red line indicates the VD. The evolution is divided into four stages of strain partitioning: 1) distributed strain and *en échelon* *R*-shear formation, 2) oblique slip on bivergent thrusts, 3) transitional strain partitioning, 4) full partitioning to throughgoing structure (s).

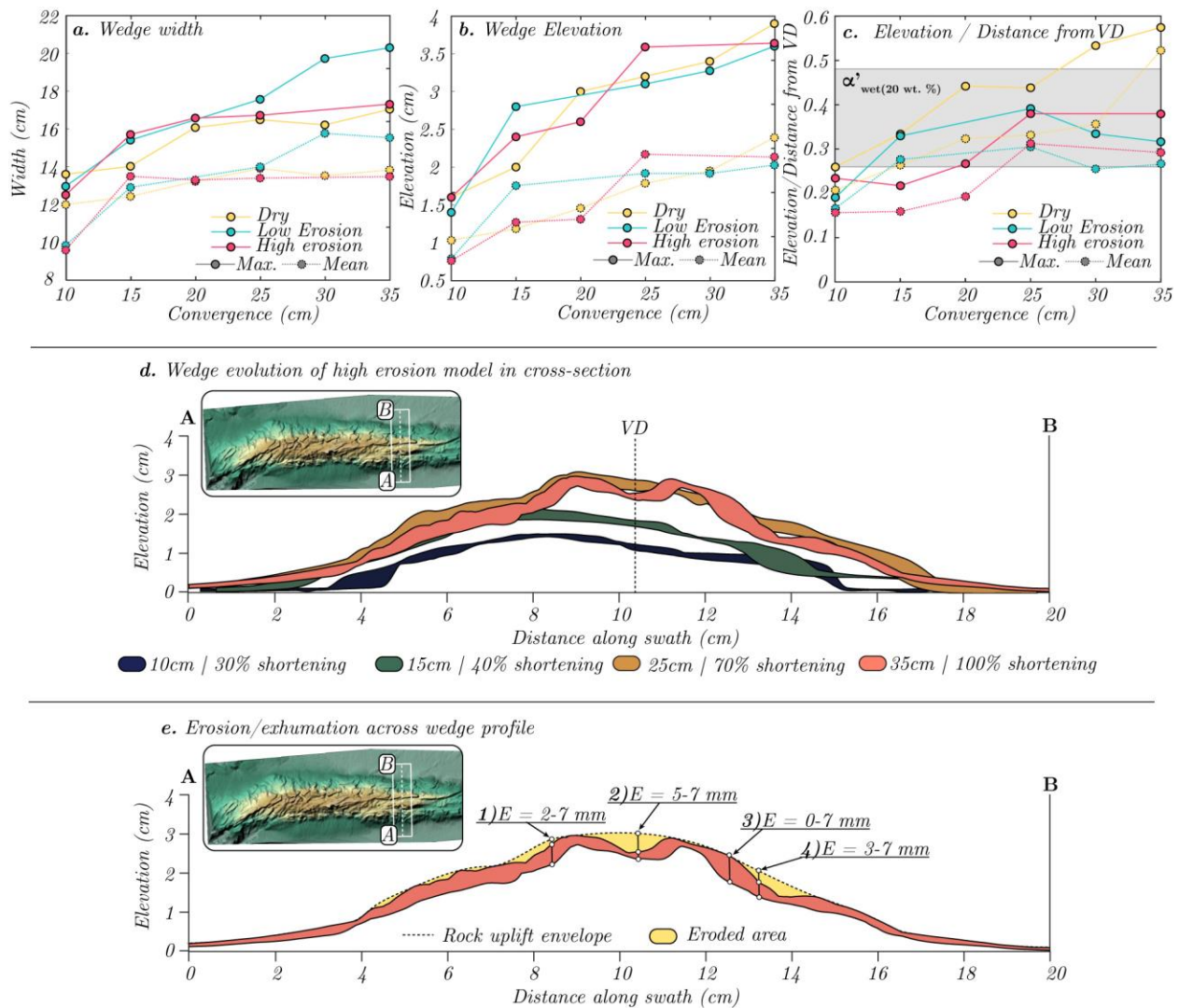


Figure 7. The topographic evolution of the presented models. (a-c) maximum and mean (a) wedge width, (b) elevation, and (c) elevation divided by the distance from the velocity discontinuity (VD). The gray bar is the error window for the theoretical wedge slope calculated from critical taper theory (see Dahlen, 1990) using the material parameters for wet (20 wt. % H₂O) CM2 from Reitano et al. (2020), α' wet. (d) Swath section showing the wedge evolution of the high erosion model. The inset shows the location of the swath at the final stage (convergence = 35 cm/shortening = 100%). (e) Estimates of exhumation across the swath taken at the final shortening stage (100%). The eroded area (yellow) is the difference

between the rock uplift envelope (dashed line) and the surface uplift (upper and lower swath bounds). Erosion/exhumation estimates, E , are the difference between rock and surface uplift (Molnar and England, 1990).

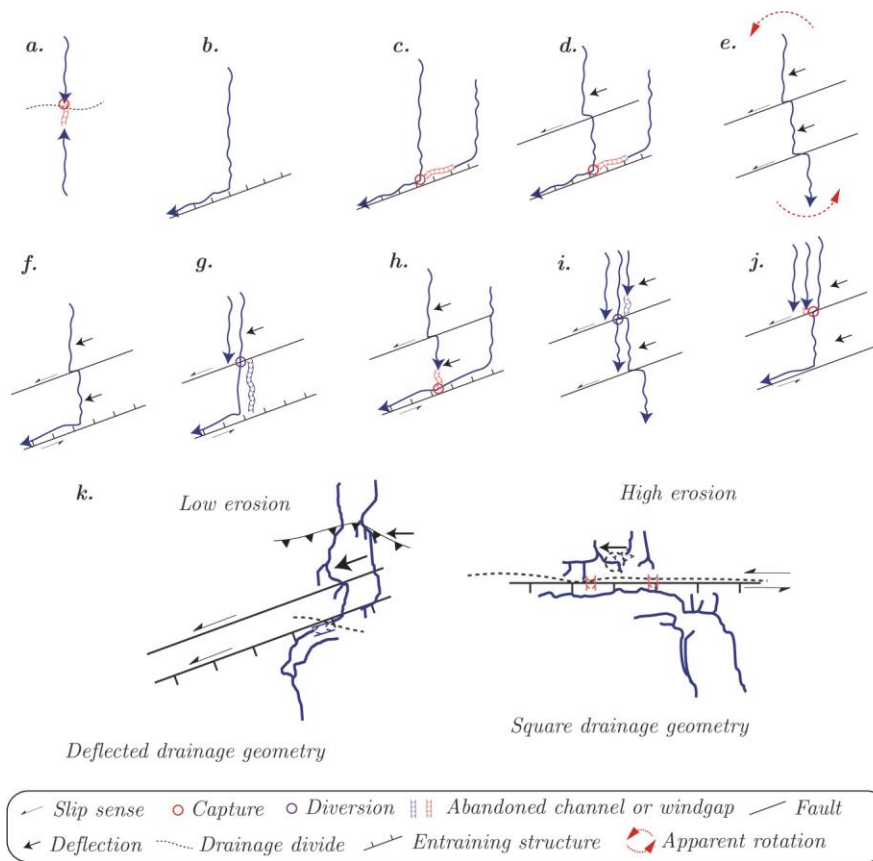


Figure 8. Examples of drainage reorganization mechanisms leading to the stream network geometries in the high and low erosion models. (a) across divide capture, (b) structural entrainment, (c) structural entrainment and capture upstream along *R*-shear, (d) deflection, entrainment, and capture upstream along *R*-shear, (e) deflection, and rotation, (f) deflection and entrainment, (g) deflection, beheading, diversion, and entrainment, (h) deflection and capture of transverse stream by stream along *R*-shear, (i) deflection, diversion, and beheading, and (j) deflection, diversion, beheading, and entrainment. (k) shows representative streams extracted from high and low erosion DEMs and, thus, how these mechanisms may combine to dictate differences in drainage patterns between models. It is evident that the structural evolution impacts the drainage geometry forming more rectangular drainages in the high erosion model.

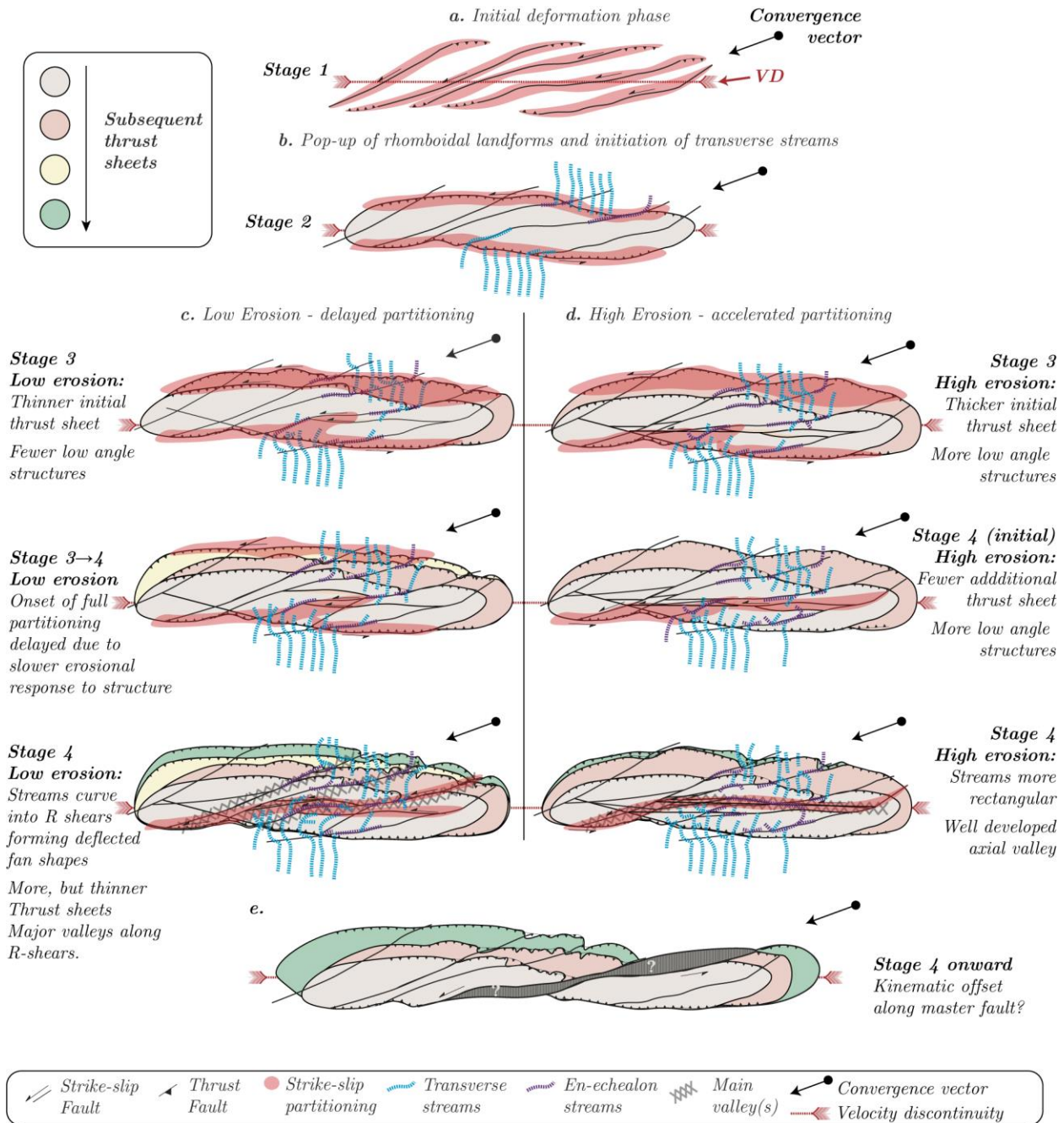


Figure 9. Illustration highlighting the differences between the evolution of fault and stream networks, strain partitioning, and topography. (a) The initial deformation phase. (b) Beginning stages of wedge development. (c) Stages 3 (transitional) – 4 (full partitioning) for low erosion systems. (d) Stages 3 (transitional) – 4 (full partitioning) for high erosion systems. (e) Wedge development after full partitioning, including potential kinematic offset.

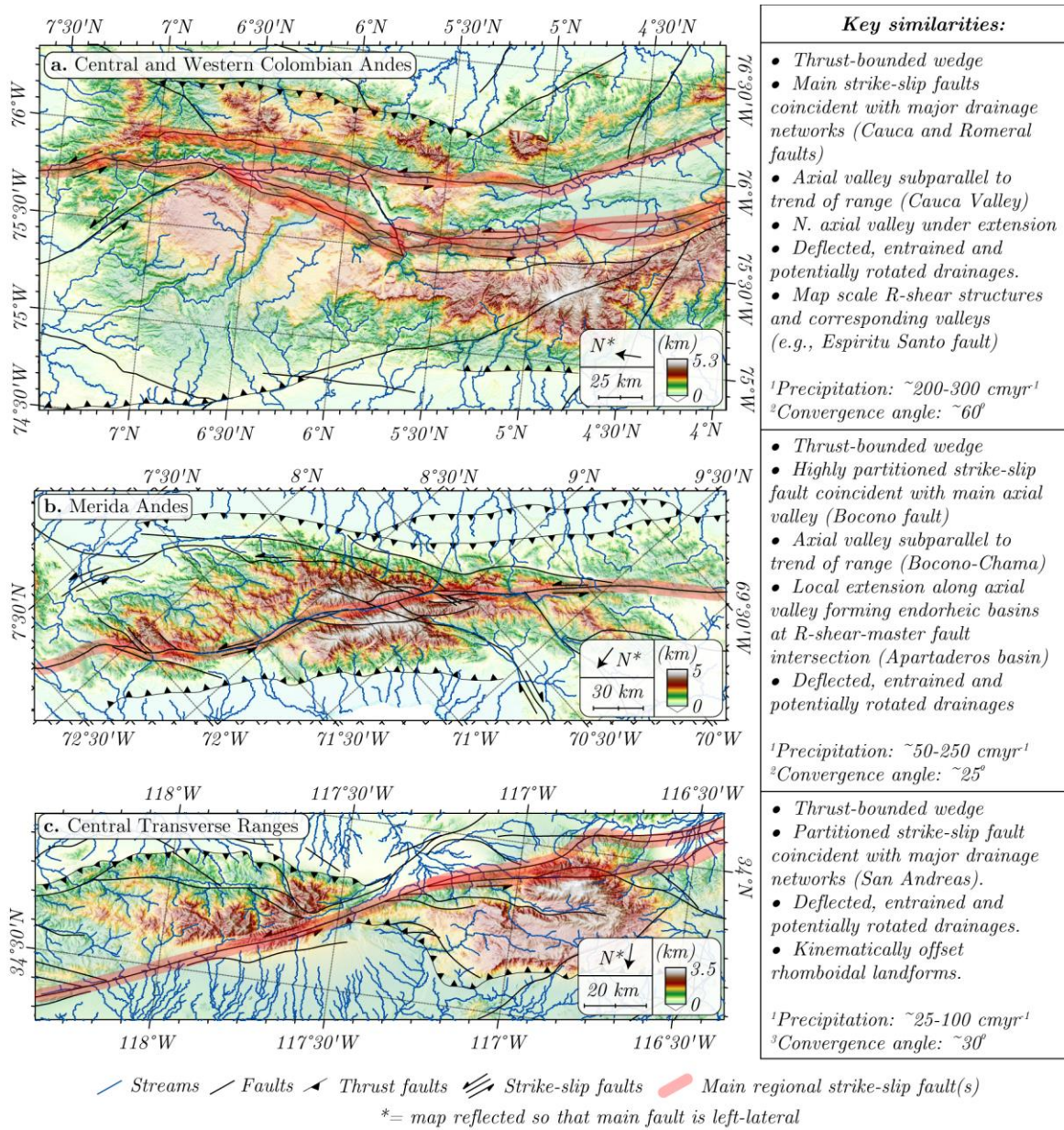


Figure 10. Natural prototypes with similar morphostructural characteristics as our models.

(a) The Merida Andes in Venezuela. (b) The Central Transverse Ranges along the San Andreas Fault north of Los Angeles, California. (c) The Central and Western Colombian Andes. The similarities between each setting and the models are listed in the boxes on the right of the figure. Precipitation data are derived from *WorldClim2* (Fick and Hijmans,

2017), and convergence angles are estimated from GPS velocity-derived kinematic block models by Mora-Paéz et al. (2019) for the northern Andes and from McCaffrey (2005) for the central Transverse Ranges.

Experiment #	Convergence Angle (°)	Convergence rate (mm/hr)	1 σ	Rainfall rate (mm/hr)	1 σ	CR	Referred to in text as:
D_62422	20	320	40			Inf.	"Dry"
W_62321	20	240	9	20	6	12	supplemental material
W_71321	20	230	11	31	13	7	"Low erosion"
W_70221	20	80	14	26	11	3	Supplemental material
W_62722	20	70	24	34	11	2	"High erosion"

Table 1. All experiments conducted using the sandbox set-up. Prefixes D and W denote wet and dry experiments, respectively. The CR is the ratio between convergence and rainfall rates.